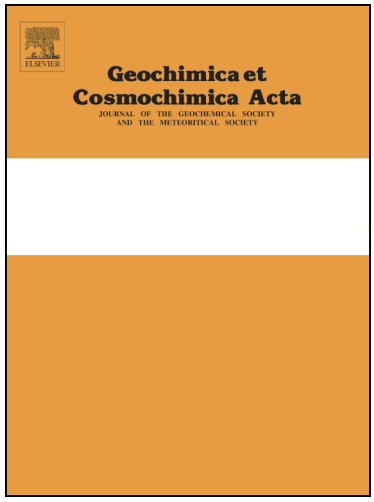

Martian low-temperature alteration materials in shock-melt pockets in Tissint: Constraints on their preservation in shergottite meteorites

C.R. Kuchka, C.D.K. Herd, E.L. Walton, Y. Guan, Y. Liu

PII: S0016-7037(17)30260-0
DOI: http://dx.doi.org/10.1016/j.gca.2017.04.037
Reference: GCA 10262

To appear in: *Geochimica et Cosmochimica Acta*

Received Date: 24 June 2016
Accepted Date: 28 April 2017

Please cite this article as: Kuchka, C.R., Herd, C.D.K., Walton, E.L., Guan, Y., Liu, Y., Martian low-temperature alteration materials in shock-melt pockets in Tissint: Constraints on their preservation in shergottite meteorites, *Geochimica et Cosmochimica Acta* (2017), doi: http://dx.doi.org/10.1016/j.gca.2017.04.037

Martian low-temperature alteration materials in shock-melt pockets in Tissint: Constraints on their preservation in shergottite meteorites

C. R. Kuchka[1*], C. D. K. Herd[1,**], E. L. Walton[1,2], Y. Guan[3], and Y. Liu[3,4]

[1]University of Alberta, Department of Earth and Atmospheric Sciences, Edmonton, AB, T6G 2E3, Canada

[2]MacEwan University, Department of Physical Sciences, Edmonton, AB T5J 4S2, Canada

[3]Division of Geological and Planetary Sciences, California Institute of Technology, Pasadena, CA 91125, USA

[4]Jet Propulsion Laboratory, California Institute of Technology, Pasadena, CA 91109, USA.

*Current address: University of Manitoba, Department of Geological Sciences, Winnipeg, Manitoba, R3T 2N2, Canada

**Corresponding author: herd@ualberta.ca

Revised according to Pink Blessing

Geochimica et Cosmochimica Acta

Version of: April 19, 2017

Abstract

We apply an array of *in situ* analytical techniques, including electron and Raman microscopy, electron and ion probe microanalysis, and laser ablation mass spectrometry to the Tissint martian meteorite in order to find and elucidate a geochemical signature characteristic of low-temperature alteration at or near the martian surface. Tissint contains abundant shock-produced quench-crystallized melt pockets containing water in concentrations ranging from 73 to 1730 ppm; water content is positively correlated with Cl content. The isotopic composition of hydrogen in the shock-produced glass ranges from δD = 2559 to 4422 ‰. Water is derived from two distinct hydrogen reservoirs: the martian near-surface (>500 ‰) and the martian mantle (-100 ‰). In one shock melt pocket comprising texturally homogeneous vesiculated glass, the concentration of H in the shock melt decreases while simultaneously becoming enriched in D, attributable to the preferential loss of H over D to the vesicle while the pocket was still molten. While igneous sulfides are pyrrhotite in composition ($Fe_{0.88-0.90}S$), the iron to sulfur ratios of spherules in shock melt pockets are elevated, up to $Fe_{1.70}S$, which we attribute to shock-oxidation of igneous pyrrhotite and the formation of hematite at high temperature. The D- and Cl-enrichment, and higher oxidation of the pockets (as indicated by hematite) support a scenario in which alteration products formed within fractures or void spaces within the rock; the signature of these alteration products is preserved within shock melt (now glass) which formed upon collapse of these fractures and voids during impact shock. Thermal modeling of Tissint shock melt pockets using the HEAT program demonstrates that the shock melt pockets with the greatest potential to preserve a signature of aqueous alteration are small, isolated from other regions of shock melt, vesicle-free, and glassy.

1. INTRODUCTION

Tissint, a recent martian meteorite fall from Morocco, has received much attention in the literature with respect to possible martian low-temperature (i.e., secondary) alteration products reported in its first description (Chennaoui Aoudjehane et al., 2012) and also its shock metamorphic history (Baziotis et al., 2013; Walton et al., 2014). The short terrestrial residence time of Tissint (approximately three months) in a hot desert environment means that recovered stones are in near-pristine condition, which implies that any secondary alteration products present in the meteorite are likely martian, not terrestrial. Tissint is also of interest because of its strongly shocked nature, containing numerous "black, glassy" shock melt pockets (Chennaoui Aoudjehane et al., 2012) which themselves variably contain high-pressure polymorphs (e.g., Walton et al. (2014). These shock melt pockets, as well as veins formed during shock by friction-induced melting, cross-cut what is otherwise a fairly typical olivine-phyric shergottite (Chennaoui Aoudjehane et al. 2012).

Recent studies assessing whether the signature of low-temperature alteration is preserved within Tissint have yielded contradictory results – primarily because no discrete, pre-terrestrial alteration products have been identified (e.g., Chennaoui Aoudjehane et al. 2012). Instead, the geochemistry of shock-generated glass is indicative of low-temperature alteration at or near the martian surface: trace element patterns demonstrate that shock melt glass is enriched in light rare earth elements (LREE) with a positive cerium anomaly which may be explained by oxidation to Ce^{4+} (Chennaoui Aoudjehane et al. 2012). Chennaoui Aoudjehane et al. (2012) proposed a scenario in which the Tissint basaltic host rock is emplaced in a surface flow or shallow sill; subsequent low-temperature alteration (particularly of phosphates, carriers for REE) results in secondary minerals within cracks and fractures. These secondary minerals are preferentially melted (and subsequently quenched to glass) during the impact event that ejects the rock into space; as such, only their geochemical signature now remains. Conversely, Barrat et al. (2014) characterized the bulk Tissint and shock-produced glass for major, minor, and trace elements, finding no LREE enrichment or positive cerium anomaly. To explain these contradictory findings, Barrat

et al. (2014) suggested that the Tissint samples studied by Chennaoui Aoudjehane et al. (2012) experienced minor terrestrial weathering and thus the glass had been contaminated. They argue that even with favorable fall and collection conditions such as a short pre-collection residence in a hot desert (several months to a few years), meteorites may be susceptible to significant chemical alteration by terrestrial processes (Barrat et al., 1999; Crozaz and Wadhwa, 2001; Crozaz et al., 2003). In contrast, Chen et al. (2015) found unambiguous evidence for volatiles (H_2O, CO_2, F and Cl) within impact-melt pockets in Tissint, with correlations in concentrations and isotopic compositions, and evidence for minimal, if any, terrestrial contamination. A linear correlation between water content and deuterium enrichment (Chen et al. 2015) indicates mixing between the water-poor, D-poor igneous rock and a surface volatile component with a composition similar to that measured in martian surface rocks and atmosphere (e.g., Villaneuva et al. 2015; Webster et al. 2013). Further evidence for the incorporation of a near-surface, secondary alteration component into Tissint comes from Cl isotopes: shock melt glass-rich fractions yield δ^{37}Cl values which are heavier and distinct from the igneous and bulk fractions, consistent with incorporation of a ^{37}Cl-enriched component which results from interaction of surface volatiles with martian crust (Williams et al., 2016). While the association of surface/atmospheric volatiles with impact melt pockets supports the scenario of preferential collapse of secondary alteration-bearing fractures and voids put forward by Chennaoui Aoudjehane et al. (2012), LREE-enrichment in impact-melt pockets was sought but not found by Chen et al. (2015). Thus it appears that Tissint preserves evidence of near-surface alteration in the form of some geochemical signatures (e.g., volatiles, D isotopic composition), but not others (e.g., LREE). Furthermore, only some shergottites preserve evidence for a near surface component within shock melt glass, in the form of minor or trace elements or isotopic compositions (e.g. Schrader et al., 2016; Williams et al., 2016).

The apparent disparity between studies of Tissint, and between Tissint and other shergottites, likely arises from several factors, which include: a high degree of heterogeneity in the abundance and distribution of pre-terrestrial components within the meteorites; differences in the number and distribution of impact-melt pockets; and the nature of the shock process itself. Shock melts are caused by

heterogeneous deformation and heating during shock compression, and may form by frictional heating along shear bands, collapse of pore space or shock wave collisions (Sharp and Decarli, 2006). It is well understood that shock metamorphism is a viable mechanism for implanting gases into meteorites (e.g., Treiman et al., 2000), and it has been demonstrated that the quenched or quench-crystallized shock melt in shergottite meteorites is the specific host of the martian atmosphere component (Walton et al., 2007; Chennaoui Aoudjehane et al. 2012). A possible mechanism for incorporating martian alteration products is similar to that for gas implantation – that is, the secondary alteration materials or regolith were already present in voids or fractures in the target material. Therefore, if any martian secondary alteration products are extant within these meteorites, they will likely be associated with shock-generated melt glass. Current observations, which indicate a small amount of hydrous, secondary alteration material, support this inference (Chennaoui Aoudjehane et al., 2012; Chen et al., 2015; Schrader et al., 2016; Williams et al., 2016).

The purpose of this study is to examine the mineralogy, glass and mineral compositions, and the volatile contents of Tissint shock melt pockets in order to elucidate the nature of the secondary alteration component within shock-produced glass. High-pressure polymorphs in Tissint shock-melt pockets and veins provide insights into their pressure-temperature-time variability. We use our results to elucidate the mechanism for trapping martian volatiles within shock melt pockets and the effect of post-shock conditions on the preservation potential of this material. Our results have implications for targeting other volatile-bearing shock melt pockets in Tissint, as well as in other shergottites.

2. SAMPLES AND METHODS

2.1 Tissint

Tissint is classified as a depleted picritic olivine-phyric shergottite, based on bulk trace element composition (Irving et al. 2012) and texture, and is composed of olivine phenocrysts set in a groundmass of pyroxene and shock-amorphized plagioclase (Chennaoui Aoudjehane et al., 2012). Subhedral to euhedral olivine crystals range from microphenocrysts <1 mm to megacrysts that are several mm across.

Other igneous phases present include chromite, titanomagnetite, pyrrhotite ($Fe_{1-x}S$; where x = 0 – 0.2), ilmenite, and merrillite ($Ca_9NaMg(PO_4)_7$). Apatite has been documented in minor amounts (Chennaoui Aoudjehane et al., 2012). Tissint is a strongly shocked shergottite; all precursor igneous plagioclase has been converted to maskelynite, a glass of feldspar composition retaining original grain boundaries and zoning, and numerous other high pressure phases are present within the meteorite including ringwoodite (γ-Mg_2SiO_4), ahrensite (γ-Fe_2SiO_4), stishovite (tetragonal SiO_2) and tissintite. Tissinite is a high-pressure polymorph of plagioclase, which has a defect-bearing pyroxene structure ($(Ca,Na,\square)AlSi_2O_6$), where "□" represents a site vacancy; Ma et al., 2015; Walton et al., 2014); the Tissint meteorite is the type locality for this mineral (Ma et al., 2015). Shock melt comprises a significant portion of the rock (up to 15 volume %; Walton et al., 2014), in the form of black, glassy shock veins and shock melt pockets, which cut across the igneous texture. Maskelynite is ubiquitous throughout the sample, whereas other high-pressure phases are associated with shock melt and are not found in non-veined regions of the host rock. Additional shock features include pervasive fracturing and mosaicism of pyroxene and olivine.

2.1 Samples

Three thin sections of Tissint from the University of Alberta Meteorite Collection - MET11640/2-2-1/TEP, MET11640/2-3-2/TEP and MET11640/2-3-4/TEP - were examined in this study. All sections were cut from sample MET11640, a 58.2 g stone that was among the first samples recovered in October 2011, rather than rock chips, which may be more susceptible to terrestrial alteration, as cautioned by Barrat et al. (2014). A thin, glossy black fusion crust envelopes the exterior of the stone with no obvious weathering on its surface. A low-speed saw was employed for sampling; all cutting was performed on dry samples, without the use of solvents or lubricants. Polished thin sections were prepared from these subsamples.

2.2 Scanning Electron Microscopy

Initial characterization of the thin sections using transmitted and reflected light microscopy identified areas of interest, primarily shock veins and shock melt pockets, which were subsequently investigated using a Zeiss Evo MA LaB_6 scanning electron microscope (SEM) at the University of Alberta (UAlberta). Back-scattered electron (BSE) images were used to characterize microtextures, and energy dispersive spectrometry was used to assist in mineral identification.

2.3 Raman Spectroscopy

Minerals were positively identified by matching peak positions collected with a micro-Raman spectrometer to literature data and the RRUFF Project database of Raman spectra (Lafuente et al., 2015). Raman spectra were acquired at MacEwan University using a Bruker SENTERRA instrument. The excitation laser (532 nm line of an Ar+ laser) was focused through a 50 × 1000 µm slit aperture using the 100× objective lens. The spot size for all analyses was ~1 µm. For silicates, analyses were acquired by three iterations of 2 s each with a laser power of 10 mW. For oxides and sulfides, Raman spectra were collected for three iterations of 2 s each at a reduced laser power (2 mW) to minimize risk of damaging the sulfide phases in the sample. Raman spectra were processed using the commercial spectroscopy software OPUS v. 6.5. This program was used to sum multiple exposures to achieve the final spectrum, to apply background corrections, to remove any peaks resulting from cosmic rays, and to stack the spectra so they could be displayed as a single image.

2.4 Major and mineral element composition of glasses and minerals

Major and minor element chemistries of glasses, silicates and sulfide minerals were analyzed by a JEOL 8900R electron probe microanalyzer (EPMA) at UAlberta equipped with an energy-dispersive spectrometer (EDS) and five wavelength-dispersive spectrometers (WDS). The shock-produced glasses are schlieren-rich and compositionally heterogeneous. Estimating the bulk composition for a volume of glass is therefore problematic because the sampling volumes for the EPMA analyses are smaller than a

volume that may be considered as "representative" for a given melt pocket or vein. To mitigate this, several analyses on glass were performed for each shock melt region, from which an approximate average glass composition was determined (Table 1). WDS analysis of glass used a 15 nA beam with a 15 kV accelerating voltage and a 10 µm beam diameter. Count times were 30 s per peak with a 15 s background. Natural glasses, silicates, oxides, and sulfides were used as standards. 2σ uncertainties for major elements are about 0.7 wt% for SiO_2, 0.2 wt% for Al_2O_3, FeO, MgO, CaO, and Na_2O, 0.1 wt% for TiO_2, K_2O, P_2O_5, and SO_3, 0.05 wt% for Cr_2O_3, 0.04 wt% for MnO, and 0.02 wt% for Cl and NiO. Representative data are provided in Table 1; the full dataset is found in the Electronic Annex (Table S1).

Quench-crystallized areas of shock melts are composed of sub-micrometer sized silicate crystals, and larger spheres and blebs of iron sulfide. For silicates, even a fully focused electron beam (1 µm) is too large to analyze individual crystallites. As a compromise, a beam diameter of 15 µm was employed to determine the "average" composition of glass and crystallites within discrete areas of the shock melt pockets. While this is not as good as analyzing individual phases, and each analysis area is sensitive to heterogeneities on the scale of a few microns, it is assumed to be adequate for estimating the composition for an area of ~177 µm². As with glass, a population of spots for each crystallite-rich area was analyzed to minimize the effect of local chemical variation. Analysis of iron sulfide spherules within shock melt pockets was performed using a 15 nA, fully-focused electron beam with an accelerating voltage of 15 kV. A population of larger spherules (several µm across, up to ~20 µm) were targeted by WDS. As the EPMA software reports chemistries in weight percent oxides, a sulfur-oxygen equivalency correction was performed following analysis. Representative data from crystallite-rich areas shock melt are provided in Table 1; the full dataset is found in the Electronic Annex (Table S2), along with data for iron sulfides (Table S3).

2.5 Volatile inventory and hydrogen isotope composition of glasses

Four distinct glass-containing shock melt pockets in Tissint section MET11640/2-3-4/TEP were selected for secondary ion mass spectrometry (SIMS) analysis. SIMS was used to determine the abundance of volatiles within shock melt glass including chlorine, fluorine, sulfur, phosphorus, and water (as hydrogen), as well as to determine the hydrogen isotope composition of the glass, which was successfully completed in two of the four pockets. The glass was analyzed using a Cameca IMS 7f-GEO ion microprobe, located at the Caltech Microanalysis Center at the California Institute of Technology. In order to fit into the instrument holder, the section was modified from a standard 1" × 2" slide to a 1" diameter round section, with double-thick glass. During this process, the sample was damaged and was split into two halves. Although damaged, the two halves seated properly onto the slide to which they were mounted. The section was repolished, carbon-coated, then stored within the SIMS instrument to degas under high vacuum (1×10^{-8} torr) for three days prior to analysis. During analysis, vacuum pressures were ~$2\text{-}3\times10^{-10}$ torr.

The SIMS analytical procedure used follows that outlined in Chen et al. (2015). A 5 – 6 nA, 10 µm diameter Cs^+ primary-ion beam was used for pre-sputtering. During analysis, the ion beam diameter was reduced to 2 µm. Each analysis spot was pre-sputtered for several minutes and was manually inspected by examining ion images of $^{16}O^1H^-$ and $^{12}C^-$ in order to avoid cracks and holes. Spots were pre-sputtered using a raster size of 25×25 µm. During analysis, this raster size was reduced to 10×10 µm. An electron gate limited the collection of ions from only the center 8×8 µm area. Ion species analyzed for concentration included $^{12}C^-$, $^{16}O^1H^-$, $^{18}O^-$, $^{19}F^-$, $^{30}Si^-$, $^{31}P^-$, $^{32}S^-$, and $^{35}Cl^-$. Natural and synthetic glasses following Chen et al. (2015) were used as standards. For elemental concentrations, each analysis was run for 20 cycles, with a dwell time of 1 s per species. Background levels for volatiles, estimated from repeat analyses of Tissint maskelynite in close proximity to shock melt pockets, are estimated to be about 50 ppm for water, 1 ppm for fluorine, 0.2 ppm for chlorine, and 0.2 ppm for sulfur, based on analyses performed by Chen et al. (2015) utilizing the same instrument, under similar analytical conditions, on the same meteorite. All reported data are background corrected.

For hydrogen isotopes, a primary beam current of 5 nA and a mass resolution of 550 were used. Each analysis was run for 100 cycles with a dwell time of 1 s for hydrogen and 15 s for deuterium. In order to directly compare water concentrations and δD, analysis spots for hydrogen isotopes were centered within pits excavated during analyses for volatile abundances, using H^- ion imaging; this imaging was also used to avoid contamination, e.g., from epoxy. The instrument fractionation on hydrogen isotope analysis was monitored using the StHs6/80-G standard with δD of -95 ±2 ‰ (Jochum et al., 2006), determined to be 0.984 (ratio of actual value to measured value) and used to correct the reported values. Following SIMS analysis, pits excavated by the primary ion beam were inspected in transmitted and reflected light, as well as by SEM in backscattered and secondary electron mode. Data from any spots that were found to have excavated microscopic cracks were discarded. Representative SIMS data are provided in Table 2; the full dataset is found in the Electronic Annex (Table S4).

2.6 Trace element geochemistry

Trace element abundances were determined using a New Wave UP213 laser ablation system and an iCapQ ICP mass spectrometer in the ICP-MS Laboratory at UAlberta, using the following isotopes: ^{139}La, ^{140}Ce, ^{141}Pr, ^{146}Nd, ^{147}Sm, ^{153}Eu, ^{156}Gd, ^{159}Tb, ^{163}Dy, ^{165}Ho, ^{166}Er, ^{169}Tm, ^{172}Yb, and ^{175}Lu. ^{43}Ca was analyzed as an internal standard, and for calibration with Ca concentrations determined by EPMA on the same spots. Fourteen spots from four different shock melt regions in MET11640/2-3-4/TEP, 11 spots from four melt regions in MET11640/2-3-2-TEP, and 12 spots from four shock melt regions in MET11640/2-2-1/TEP were analyzed. To compare shock melt pockets to the host rock, igneous minerals in MET11640/2-3-4/TEP were analyzed in a separate session employing identical analytical conditions, including 13 analyses on olivine, 13 analyses on pyroxene, and 10 analyses on maskelynite. Due to the paucity and small size of merrillite in the sample, one analysis was performed on a single merrillite crystal, using a reduced spot size of ~25 µm. Glass standards from the National Institute of Standards and Technology (NIST612 and NIST614) were used as standards for trace elements. Calibration was

performed using NIST SRM 614 and checked using NIST SRM 612. Each set of unknown analyses was bracketed by NIST analyses (both 612 and 614) to monitor instrument drift. To reduce interferences from oxides the instrument was tuned such that ThO/Th <0.5 %; to mitigate doubly charged species the instrument was tuned so that $^{137}Ba^{++}/^{137}Ba$ < 3 %. Molecular interferences were dealt with on an element by element basis, usually by selecting an isotope not likely to have spectral interference. Samples were ablated by a 10 Hz laser with a spot size of ~55 µm at ~9-10 J/cm^2. Each analysis was run for 60 seconds including a 25 second laser warm-up period, followed by a 20 second washout period. Dwell times for ion species were between 0.03 and 0.1 s. Representative data for REE in shock melt pockets are provided in Table 1; the full dataset is found in the Electronic Annex (Tables S5 and S6).

2.7 HEAT thermal modelling

The HEAT program (Wohletz et al., 1999), freeware thermal modelling software, was used to constrain the post-shock cooling history of the shock melt. Following the method of Shaw and Walton (2013), the distribution of shock melt in Tissint was mapped using in the ImageJ freeware image-processing software. This program was used to produce maps by assigning the products of shock melting to black pixels, vesicles within shock melt to blue pixels, and all surrounding materials "groundmass" to white pixels. This map was then plotted onto a grid within the HEAT program. The distribution of shock melt was mapped on a 0.1 mm grid. Although a grid size of 0.1 mm is smaller than the minimum grid size of 0.01 m available in HEAT, the results may be scaled down to suit the scale of the meteorite by applying a scaling factor to the data output by the program (Shaw and Walton, 2013). For one shock melt pocket, the borders of the shock melt were extrapolated beyond the edge of the thin section, as the edge of the section cuts through the center of the pocket and disrupts two vesicles that are assumed to have been originally enclosed within glass. The dimensions of the melt pocket in this case were therefore extended such that the vesicles are symmetrical and enclosed by 0.2 mm of shock melt. Regions of shock melt smaller than 0.1 mm^2 were ignored. For the model parameters, the bulk groundmass is assumed to have a

density of 3000 kg/m^3, a thermal conductivity of 1.8 W/mK (Murase and McBirney, 1973), and a heat capacity of 1000 Jkg^{-1}K^{-1} (Bouhifd et al., 2007). These values are appropriate for basalt, although we note that olivine-phyric martian basalts have slightly higher densities than included in our model (3290 kg/m^3 versus 3000 kg/m^3; Coulson et al., 2007). For additional details on the thermal modeling see Shaw and Walton (2013). Shock melt is assumed to have a density of 2725 kg/m^3, a thermal conductivity of 2 W/mK, and a heat capacity of 1500 Jkg^{-1}K^{-1}. The initial temperatures were 2500 °C for shock melt and 500 °C for the groundmass. The melt temperature was taken as 2500 °C which is just above the solidus of basalt at 20–25 GPa (Wang and Takahashi, 1999; Hirose and Fei 2002). The temperature assigned to the groundmass (500 °C) is an estimate of the post-shock temperature based on the calculations of Beck et al. (2007), which take into account energy dissipated by void collapse and estimated pre-shock porosity of martian basalts. For the purposes of the model, vesicles are assumed to be filled with air, with a bulk density of 1.12 kg/m^3 and a heat capacity of 1004 Jkg^{-1}K^{-1}, with an initial temperature of 500 °C, the same as the groundmass temperature. Calculations were run until all melt had cooled to 900 °C, the approximate temperature of the basalt solidus (Shaw and Walton, 2013). Results of modeling are presented and discussed below, with further details provided in the Electronic Annex (Figures S1-S3).

3. RESULTS

3.1 Composition, mineralogy and microtexture of shock melts

Shock melt in Tissint is observed as shock veins and shock melt pockets (Figure 1; Chen et al. 2015; Liu et al. 2016). Shock veins typically cut across and displace igneous minerals but also follow grain boundaries. Shock melt pockets vary in size (from <0.1 mm^2 to >3 mm^2), morphology (rounded to amoeboid), and crystallinity (glass to quench-crystallized). Some shock melt pockets have quenched to compositionally homogenous or schlieren-rich glass, others have quench-crystallized with equant euhedral to skeletal silicate microcrystals. Oxides and small (<1 µm to ~20 µm), spherules of iron sulfide are typically observed within shock melt in varying abundance. Shock melt pockets have a tendency to

"coarsen" inwards: crystallinity and crystal size increase towards the center of the pocket or vein. A gradation is typically observed from glass to crystallites to microscopic crystals ~2–10 μm in size. The largest shock melt pocket (~3.5 mm^2) contains dendritic crystals of pyroxene up to 80 μm in length. The exception to this trend in crystal size is when vesicles are present: vesicles are enveloped by glass, and crystallinity increases away from the vesicle (Fig. 1a).

Several shock-induced phase transformations are documented in host rock minerals adjacent to, and entrained as clasts within, shock melt. Ringwoodite and tissintite were identified based on peak positions in acquired Raman spectra (Figs. 1, 2). A doublet near 793 cm^{-1} and 842 cm^{-1} corresponds to the expected vibrational modes for ringwoodite. Tissintite has two occurrences: as crystals + plagioclase glass entrained as clasts within shock melt pockets, and as a "border" within amorphous glass of plagioclase composition in direct contact with shock melt (Fig. 1c and d). Raman spectra exhibit peaks at ~380, 693, and 997 cm^{-1} (Fig. 2), consistent with those spectra reported for tissintite by Walton et al. (2014) and Ma et al. (2015).

The composition of glass within shock melt pockets (Tables 1, S1) is heterogeneous on a micrometer-scale in major and minor elements, consistent with previous observations from Tissint and other shergottites (e.g., Chen et al. 2015; Walton et al. 2010). Aluminum and calcium abundances are correlated, and these elements are anti-correlated with magnesium and iron. High Al_2O_3 (>8 wt%) and high CaO (>10 wt%) correspond to schlieren or flow-textured blebs within the glass that appear darker (lower density in BSE images) than average glass (Figure 3). EPMA analyses of crystallite-rich regions agree, within uncertainties, with those regions that consist entirely of homogeneous glass (Tables 1, S1-S2). No clear, well-defined signals for Cl were detected using quantitative EPMA. Likewise, EPMA X-ray elemental maps demonstrate that there are no significant excesses (or "hot spots") of Cl, F, or P associated with the shock melt glass (Fig. 3); neither were S hot spots found within shock melt glass. Some fluorine is detectable by X-ray mapping within cracks and holes in the section (Fig. 3); this excess fluorine is attributable to epoxy and is not intrinsic to the rock. EPMA X-ray maps (specifically Ca, Na, Mg, and P) were also used to identify merrillite in the igneous host rock, which is present in relatively

low abundance (<1 %) as small grains (up to ~35 μm); identification of merrillite was confirmed by Raman spectroscopy with peak positions near 957 cm^{-1} and 973 cm^{-1} (Fig. 2a).

3.2 Sulfides associated with shock melts

Results of our analyses of sulfides by SEM, EPMA and Raman indicate that spherules within shock melt pockets are distinct in terms of texture and composition from the igneous iron sulfides. Host rock (igneous) iron sulfides have an average composition corresponding to $Fe_{0.89}S$. In contrast, spherules within the shock melt have elevated iron to sulfur ratios, above that of troilite (FeS) (Fig. 4; Table S3). Raman spectra collected on host rock pyrrhotite exhibit two strong peaks at 330 cm^{-1} and 380 cm^{-1} while those spectra from iron-sulfide spheres within shock melt contain additional peaks at 218 cm^{-1} and 282 cm^{-1} (Fig. 2a). These peak positions, which are not observed as a spectral signature of igneous pyrrhotite, are characteristic of hematite. Sulfide spherules that exhibit these additional Raman peaks correspond to those same grains with elevated Fe:S ratios, determined by EPMA. Thus, EPMA and Raman results are consistent with a mixture of pyrrhotite and hematite in the shock melt spherules.

3.3 Water abundance and isotopic composition in shock melt glass

Water content in Tissint shock melt pockets is highly variable, ranging from 73 to 1730 ppm within and between regions of shock melt in MET11640/2-3-4/TEP (Tables 2, S4). Water is positively correlated with chlorine, only weakly correlated with fluorine, and not correlated with phosphorus or sulfur (Fig. 5). δD values in Tissint glass range from ~2600 ‰ to ~4340 ‰ (Table 2), consistent with a martian origin. δD is negatively correlated with $1/H_2O$ (Fig. 6). In one shock melt containing homogeneous glass, ion probe traverses reveal that water content decreases and δD increases as a large vesicle is approached (Figs. 6, 7).

3.4 Trace element concentrations in shock melt pockets and host minerals

Results for REEs from LA-ICP-MS analyses are shown in Figure 8 and provided in Tables 1, S5 and S6. Data were normalized against elemental abundances in CI chondrites reported by Palme et al. (2014). The abundances of REE in the major minerals in Tissint (Fig. 8, Table S5) are consistent with what is expected based on known partitioning behavior, and with previous studies (e.g., Balta et al., 2015, Liu et al., 2016): abundances are lowest for olivine; pyroxene and maskelynite have similar abundances, although a positive europium anomaly is present for maskelynite; and abundances are greatest in merrillite. Pyroxene, olivine, and maskelynite are depleted in LREE, which is typical for depleted shergottites. Although only one merrillite analysis was possible, results are generally consistent with REE reported for Tissint merrillite (Balta et al., 2015; Liu et al. 2016). Our results for shock melt REE (Fig. 8, Table S6) are comparable to those previously reported (Chennaoui Aoudjehane et al., 2012; Barrat et al., 2014; Balta et al., 2015; Liu et al., 2016). There is no discernable difference in the REE concentrations of shock melt, whether texturally homogeneous and glassy, or crystallite-rich with interstitial glass (Fig. 8); furthermore, REE concentrations are similar between shock melt analyzed from different thin sections. Tissint shock melt REE concentrations are comparable to those obtained for maskelynite (Fig. 8), and show depletion in LREE. No LREE enrichment or positive cerium anomaly were observed in any Tissint shock melt.

3.5 Cooling history of shock melt pockets modelled by HEAT

We mapped the distribution of shock melt within the three thin sections (Figure 9), and used these as initial conditions for modeling using the HEAT program. Seven modelled melt pockets, the largest being ~0.5 mm^2, were modeled in section MET11640/2-3-4/TEP (Figs. 9, S1); HEAT results calculate this melt cooled completely to the solidus in 0.14 s. Section MET11640/2-3-2/TEP (Figs. 9, S2) contains slightly more melt volume with larger shock melt pockets relative to section MET11640/2-3-4/TEP, and cooled to the solidus in 0.50 s. Section MET11640/2-2-1/TEP (Figs. 9, S3) contains the highest abundance of shock melt compared to the other sections modelled; the melt in this section cooled much

slower, with the melt cooling to the solidus within 2.60 s. Within this section, small isolated pockets cooled very quickly. In contrast, heat persisted near the center of the section, where the thermal haloes from several large, closely-spaced melt pockets constructively interfered.

Notably, areas that contain dendrite-poor or dendrite-free glass correspond to those areas that cooled the fastest based on our modeling. The largest skeletal and dendritic crystals of olivine and pyroxene are correlated to those regions in the model that remained above the solidus for extended periods of time; for example, relatively large dendritic crystals are seen within the center of large pockets of MET11640/2-2-1/TEP (Figure 10). Shock melt pockets containing vesicles cooled considerably faster than vesicle-free shock melt pockets of similar size. Modeling demonstrates that shock melt adjacent to a vesicle will solidify first, and that the solidification front will radiate outward from the vesicle.

4. DISCUSSION

4.1 Major, minor, and trace elemental compositions of shock melt pockets

Shock melt glass is basaltic in composition, consistent with its derivation from local igneous phases through melting, as observed previously (e.g., Chen et al., 2015; Liu et al., 2016; Walton and Herd, 2007; Walton et al. 2010). Thus, the major and minor elemental compositions of silicate glass and crystallites within shock melts in Tissint reflect the melting and incorporation of local igneous minerals in varying abundances. Aluminum and calcium locally co-vary (Fig. 3), as do iron and magnesium; this covariance may be attributed to the melting, incorporation and incomplete mixing of the major igneous silicate minerals - namely plagioclase, pyroxene, and olivine – to specific spots within a melt pocket, leading to compositional heterogeneities. In all cases where examined by EPMA, chlorine was below the limit of determination (<0.1 wt%), and no "hot-spots" of chlorine, fluorine, or phosphorus were detected. X-ray elemental maps, WDS and EDS analyses on shock melt pockets suggest an absence of significant igneous apatite incorporated within Tissint shock melt glass; Chen et al. (2015) came to the same conclusion based on their analyses. All phosphates detected in this study contain significant sodium and

magnesium, with a doublet in Raman spectra centered at 957 and 973 cm^{-1}, characteristic of merrillite (Fig. 2a). Potassium contents of shock melt pockets (0.03 ± 0.03 wt% K_2O; Table S1) are comparable to that reported for the bulk rock (0.02 wt% K_2O; Chennaoui Aoudjehane et al., 2012); there is no evidence for incorporation of significant amounts of a K-rich alteration phase such as jarosite ($KFe^{3+}_3(OH)_6(SO_4)_2$).

REE abundances in shock melt pockets can also be explained by melting of igneous phases in Tissint. Shock melt pockets are depleted in LREE (Fig. 8), and parallel the REE pattern observed for the bulk rock (cf. Chennaoui Aoudjehane et al. 2012; Barrat et al. 2014; Liu et al., 2016). Shock melt pocket REE can be explained by local melting of igneous phases, which themselves are depleted in LREE (Fig. 8), although the higher overall abundance of the REE (especially the HREE) relative to the dominant igneous phases (pyroxene, olivine, or maskelynite) requires the incorporation of a small (< 0.5 %) amount of merrillite – the main REE carrier – into the shock melt. In agreement with the results of Barrat et al. (2014), a cerium anomaly is not observed for Tissint shock melt pockets, nor is an enrichment in the LREE relative to the host igneous minerals. Therefore, an extraneous LREE-bearing component is not required to explain the REE patterns of Tissint shock melt pockets.

4.2 Hematite as evidence for oxidation during shock metamorphism

Terrestrial alteration of meteorites can result in secondary mineralization, including the formation of hematite, even in hot deserts in a relatively short time (e.g., tens of years; Barrat et al., 1999); however, it is unlikely that Tissint experienced significant weathering during its 3-month residence on Earth prior to collection (Chennaoui Aoudjehane et al., 2012). Indeed, Balta et al. (2015) provide arguments for the lack of terrestrial alteration based on trace element considerations. Hematite, identified by peaks near 218 and 282 cm^{-1} in Raman spectra (Fig. 2a), is only present within shock melt pockets where it is associated with sulfide spherules; these Raman peaks are absent in igneous pyrrhotite (Fig. 2a). Of the two shock melt pockets analyzed for H isotopic composition and which show D- and Cl-enrichment (section 4.3), hematite was found in one of them.

We consider the possibility that the analyzed sulfides were oxidized in the course of Raman analysis. The oxidation of pyrrhotite by a Raman laser has been demonstrated for laser powers of 25 mW in an oxidizing environment (normal air, Mernagh and Trudu, 1993; Avril et al., 2013). After subjecting individual grains of pyrrhotite to repeated exposure to our 2-mW Raman laser or allowing the laser to dwell on the mineral for several minutes, no change in the Raman spectrum was observed. It is also significant that igneous pyrrhotite was analyzed under the same conditions, yet peaks in Raman spectra indicative of hematite were not observed. Oxidation of iron sulfides as an artefact of the analytical technique can therefore be ruled out.

Hematite has been documented in other shergottites by using Raman spectroscopy, e.g., EETA79001 (Wang et al., 2004a; Wang et al., 2004b). Hematite has also been identified in another martian fall, Zagami, as grains adjacent to pyrrhotite (Wang et al., 1999). In both EETA79001 and Zagami, it has been suggested that the hematite is martian (Wang et al., 1999; Wang et al., 2004a; Wang et al., 2004b).

Sulfide spherules are common within shergottite shock melt glass, and are interpreted to be derived from melting of igneous sulfides due to their high compressibility and low melting temperature relative to other minerals (Ross et al., 2013; Walton et al., 2010). Sulfides become incorporated immiscibly into the silicate melt (Walton et al., 2010). Sulfide spherules within Tissint shock melt glass, however, are chemically distinct from igneous sulfides from which they are derived. Iron to sulfur ratios for sulfides within shock melt pockets are elevated relative to those in the regions of the rock that did not experience shock melting (Fig. 4), implying that the sulfides were modified after igneous crystallization. Altered Fe/S in shock-metamorphic sulfides has been observed in Tissint and other shergottites (Ross et al., 2013; Sutton et al., 2014). Ross et al. (2013) hypothesized that an additional precursor component – namely, a trapped sulfate (e.g., jarosite) – within the shock melt was reduced to sulfide during shock. However, given the relatively high water content within Tissint shock melt pockets (in some cases >2500 ppm) and that the Amazonian atmosphere is relatively oxidizing, not reducing, shock oxidation is more likely than shock reduction. Additionally, EPMA and SIMS analyses on Tissint shock melt glass

undertaken in this study do not provide evidence for a significant jarosite component, which would be detectable by excess potassium, sulfur and water.

Hematite is not a phase that is expected to be in equilibrium with the igneous host rock, as it would indicate a much higher oxygen fugacity than that recorded by the Fe-bearing phases (olivine, pyroxene, spinel and iron-titanium oxides) which crystallized from the Tissint parent melt. Based on equilibria among these minerals, the igneous crystallization conditions for Tissint were initially 3.5 to 4 log units below the quartz-fayalite-magnetite (QFM) buffer (QFM – 3.5 to – 4; Balta et al. 2015; Castle and Herd, 2017), rising to a maximum of QFM – 1.4 for the latter stages of crystallization (Castle and Herd, 2017). Even the late-stage conditions are significantly lower than the oxygen fugacity required to allow the formation of hematite (above the magnetite-hematite, MH, buffer, equivalent to ~QFM + 6). As such, the formation of hematite simply by melting local igneous phases and incorporating them into a shock melt pocket before solidification may be ruled out; some event is necessary to raise the oxygen fugacity relative to that in the igneous host rock. The oxidizing event that allowed for the formation of hematite was likely associated with the formation of the shock melt pockets because of the spatial association between this mineral and shock melt documented in this study. The source of the oxidizing agent may be martian atmosphere within open pores or fractures in the pre-shocked rock. Alternatively, if the cracks and fractures within the rock were infiltrated by water, shock-loading may induce localized hydrothermal alteration, including the oxidation of iron (Kieffer and Simonds, 1980; Feldman, 1994). Hematite is readily produced during modeling of impact-induced hydrothermal alteration at high water/rock ratios under conditions relevant to Mars (Schwenzer and Kring, 2009; Filiberto and Schwenzer, 2013; Schwenzer and Kring, 2013). Another possibility is that the hematite formed by aqueous alteration prior to the formation of the shock melt pockets, and its origin is unrelated to shock metamorphism. However, since the iron-bearing phases in the groundmass show no signs of significant alteration (from textures or major and minor element compositions), and sulfides with elevated Fe/S values are restricted to shock melt pockets and veins, we conclude that shock oxidation is more likely. Notably, pyrrhotite will oxidize to hematite (via magnetite) at temperatures >450 °C (Dekkers, 1990)

under oxidizing conditions; such temperatures are easily exceeded during shock melt pocket generation (Sharp and DeCarli, 2006; Spray and Walton, 2013; Walton et al., 2010).

4.3 The volatile inventory of Tissint shock-produced glass

The bulk of the Tissint meteorite is composed of nominally anhydrous minerals (NAM) dominated by pyroxene, olivine, and plagioclase (now maskelynite). Water contents for these minerals in Tissint were estimated by Chen et al. (2015) to be 0 ppm for olivine, 0−100 ppm for plagioclase, and 500−600 ppm for pyroxene, with an average for Tissint NAMs of ~200 ppm H_2O. Thus, water contents within Tissint shock melt pockets (up to 1730 ppm H_2O) are much higher than in the igneous proportion of the rock. To explain elevated water abundances a hydrous phase must have been preferentially incorporated into the shock melted proportion of the rock. Significant contribution of water to shock melt pockets by preferential melting of hydrous igneous minerals is unlikely because the only nominally hydrous mineral present within the meteorite is apatite, and only in trace amounts (Chen et al. 2015; Chennaoui Aoudjehane et al., 2012). The only phosphate phase documented here is merrillite, which is nominally anhydrous; while our results demonstrate the involvement of merrillite in shock melt pocket formation, the fluorine, chlorine, and water contents of the shock melt pockets cannot be explained by the incorporation of merrillite alone.

Within all shock melt pockets analyzed, chlorine is correlated with water (Fig. 5a), as Chen et al. (2015) noted, suggesting that chlorine accompanied water when originally introduced to the rock. This positive correlation with water is only weakly observed for fluorine and not observed for sulfur or phosphorus (Fig. 5; see also Chen et al. 2015). Igneous apatite has been ruled out as the main source of the water within the shock melt pockets, as there would be a positive correlation of phosphorus with the volatile components F, Cl, and H_2O (Fig. 5d; Chen et al., 2015). Instead, the water and chlorine in Tissint shock melt pockets is most likely a remnant geochemical fingerprint of aqueous alteration processes on Mars.

Hydrogen isotopic results provide further insights into the nature of the hydrous material. Ion probe analyses demonstrate that δD values in Tissint shock glass plot along a negatively sloping line when plotted against $1/H_2O$ (Fig. 6), similar to the relationship observed by Chen et al. (2015). This negatively sloping trend most likely represents a mixing line between two isotopic reservoirs. The water-poor, low-δD reservoir is likely derived from the igneous mineralogy of the rock (Chen et al. 2015), which inherited an isotopic signature that reflects the martian mantle. While estimates for the martian mantle vary (e.g., Usui et al., 2012, 2015; McCubbin et al. 2016), Filiberto et al. (2016) provide arguments for adopting δD = -100 ‰ and ≤ 200 ppm H_2O for martian mantle sources. Our regression line yields 146 ppm H_2O assuming δD = -100 ‰ (Fig. 6), consistent with the recommended value when uncertainties are taken into account. Notably, the intermediate δD reservoir (~1000-2100 ‰) with relatively high water contents (> 500 ppm) observed in other martian meteorites by Usui et al. (2015) is not observed in our data; nor is it indicated by the dataset of Chen et al. (2015). We can therefore conclude that this intermediate reservoir is not involved in the petrogenesis of the Tissint shock melt pockets. Furthermore, we do not observe a correlation between δD and Cl (Table S4) which would indicate the involvement of D-enriched apatite (representative of late-stage magmatic water; Usui et al. 2015). The second hydrogen reservoir in our data is near-surface water with an elevated δD of ~6900‰ (based on the y-intercept, Fig. 6). This high δD is consistent with water from the martian surface which is readily exchanged with atmosphere (e.g., Jakosky and Jones, 1997; Greenwood et al., 2008; Hu et al., 2014; Usui et al. 2015). *In situ* measurements by the Curiosity Rover suggest that martian surface and atmospheric waters have δD values in excess of 5000 ‰, and that water near the poles of Mars may have δD values as high as 7000 ‰ (Webster et al., 2013; Villanueva et al., 2014).

While our results confirm and extend the results of Chen et al. (2015) for Tissint, it is notable that two data points lie away from the others on the plot δD vs. $1/H_2O$ line (Fig. 6). The context for these points is important - they were collected from shock melt glass in close proximity to a large vesicle (Fig. 7). Furthermore, they are correlated with a lower abundance of water within this specific melt pocket: glass becomes drier (Fig. 7) and enriched in the heavier isotope (cf. Fig. 6) as the large vesicle is

approached (Fig. 7). It has been demonstrated experimentally that impact-induced devolatilization will cause the fractionation of hydrogen isotopes, in which hydrogen is preferentially partitioned into the released gas (Tyburczy et al., 2001). This mechanism is likely responsible for the trend observed in the shock melt pocket highlighted in Figure 7; specifically, the preferential partitioning of isotopically lighter water into the vesicle while the shock melt pocket was molten.

High δD values also rule out significant terrestrial weathering. For all data collected, no data plot below the line towards water-rich, low δD region. Any terrestrial alteration (for example, by dew percolating into cracks) would spread data towards a low δD and low $1/H_2O$ (Fig. 6). Our data for Tissint demonstrate an absence of terrestrial weathering, and the volatile signature preserved within the shock-produced glass is therefore martian, and not terrestrial.

4.4 Crystallization of shock melt pockets in Tissint

A coarsening progression, with the finest crystallites (or glass) at the margins and the coarsest crystals near the center, is observed in Tissint shock melts. This texture is consistent with cooling by conduction of heat to the colder host rock (Walton and Herd, 2007; Shaw and Walton, 2013). Additional nucleation sites were provided by incorporation of relatively cold lithic and mineral fragments into the shock melt, concentrated near the margins. These colder clasts served as heterogeneous nucleation sites from which zoned crystals radiate. Shock melt therefore quenches first at the margins where it is in contact with colder host rock, as well as around lithic fragments. The center of the melt stayed molten longer and cooled more slowly, which allowed for the nucleation and growth of larger crystallites. The exception to this crystallization trend occurs when vesicles are present within the shock melt pocket. In those shock melt pockets that contain vesicles, the vesicles are enveloped by homogeneous or schlieren-rich glass, indicating that these regions cooled more rapidly than those areas lacking vesicles. Even in large mm-size shock melt pockets, those areas near vesicles cooled very rapidly, more rapidly than would be explained by conduction to the colder host rock. Volatiles may be important in this case, as degassing

increases the solidus temperature, causing the melt to reach the solidus more quickly. In MET11640/2-2-1/TEP, our modeling shows that, in the largest regions of shock melt, the melt quickly quenches around vesicles, cools rapidly near the margins with the host rock, and cools relatively slowly in portions in the shock melt pocket interior, where the largest crystallites are found (Fig. 10).

4.5 Shock-induced phase transformation

Transformation of plagioclase to maskelynite is common in strongly-shocked meteorites, including the majority of martian meteorites (e.g., Rubin, 2015). The high-pressure phases present in Tissint (ahrensite, ringwoodite, maskelynite, tissintite, stishovite, and amorphized bridgmanite + magnesiowüstite) formed by solid-state transformation of precursor igneous minerals or by crystallization from impact-produced melt (e.g., Arhens et al., 1969; Ma et al., 2015; Tschauner et al., 2014; Walton et al., 2014, Jaret et al., 2015). These phases constrain shock pressures to >19 GPa but <30 GPa (Walton et al., 2014). The association between high-pressure phases and shock melt is well documented from meteorites; for example, ringwoodite in highly-shocked meteorites typically occurs as lamellae within larger olivine crystals adjacent to melt pockets or veins (e.g., Xie et al., 2006; Beck et al., 2005; Walton et al., 2014). Evidence for olivine-to-ringwoodite transformation in Tissint from petrographic observations or Raman spectroscopy was not observed in olivine distal to shock melt pockets. The reason for this may be that despite the high pressures experienced by the bulk rock during the passing of the shock wave, additional heat from the shock melt was required to overcome the energy barrier to allow for the solid-state transformation from olivine to ringwoodite and ahrensite (Walton et al., 2014).

Tissintite is observed within the center of former plagioclase clasts entrained within shock melt pockets, and as small grains within plagioclase glass along the margins of shock melts. The same mechanisms may apply with tissintite as with olivine polymorphs wherein excess heat from the shock event is required to overcome the activation energy. The pressure required for phase transformation is indeed temperature-dependent – at elevated temperatures, transformation of plagioclase to high-pressure

phases such as maskelynite, jadeite, and garnet may proceed at lower pressures (Kubo et al., 2010). Similar to jadeite, transformation of maskelynite to tissintite is facilitated by high post-shock temperatures where the hotter portion of the grain in direct contact with the shock melt is preferentially transformed (Fig. 1d). Residual energy from the shock event (or "waste heat") may allow for the back-transformation; in Tissint, the exterior of the clasts within shock melt pockets may have back-transformed to maskelynite, while the center of the clasts were somewhat insulated from the high post-shock heat (Fig. 1c). In either case, crystallization must have been rapid, at high pressures, before the pressures generated from the propagating shock wave had completely dissipated. The preservation of high pressure polymorphs and the crystallization of the shock melt pockets are thus closely related.

5. SUMMARY AND IMPLICATIONS

Shock-produced melt pockets in Tissint, a recent martian meteorite fall, have been investigated using an array of analytical techniques with the purpose of identifying martian alteration products associated with these features. Data from EPMA and LA-ICP-MS analyses suggests that there has not been any appreciable incorporation of a near-surface component (e.g., soil, jarosite, etc.) that may be detected through quantification of major and minor element abundances. Trace elements, especially the REE, are consistent with shock melting of igneous phases, with no exogenous component required to explain REE patterns of shock melt. In contrast, Cl and H_2O concentrations and D isotopic composition indicate the trapping of a component derived from the martian near-surface. Hydrogen isotopes confirm that the geochemical signature within Tissint shock melt cannot be attributed to terrestrial contamination. Water in Tissint melt pockets represents mixing from two H isotope reservoirs, a relatively dry, low-δD Mars mantle reservoir, and a high-δD Mars surface water reservoir.

Some, but not all, shock melt pockets in Tissint contain a geochemical signature characteristic of martian low-temperature alteration products. The distribution of such melt pockets is likely heterogeneous within the host rock as cracks and voids that hosted these alteration products preferentially melted as the

shockwave passed through the rock, inducing void collapse. In contrast, no such signature would be expected within a shock melt that formed from friction-induced melting along the boundaries of igneous phases, distal to any open cracks or fractures containing surface-derived components. The initial distribution of martian weathering products in the pre-shocked rock was also presumably heterogeneous, contributing to the heterogeneous distribution of incorporated low-temperature components therein. Hematite in Tissint is inferred to result from the alteration of pyrrhotite in a hot, locally-oxidized environment, i.e., during the impact shock event. As shock melt glass is pervasive, the identification of hematite (using a rapid and non-destructive technique such as Raman spectroscopy) may prove useful for prioritizing regions of interest to search for martian low-temperature alteration components in shergottites, although we note that a correlation between the presence of pyrrhotite altered to hematite, and D- and Cl-enrichment has yet to be firmly established, and requires further investigation.

The preservation of the D-, Cl-rich component – if present – depends on the subsequent cooling history of the shock melt pocket, which is dependent on its size, geometry, proximity to other shock melt pockets, and by the presence or absence of vesicles. Preservation is maximized in small, isolated melt pockets, which quench rapidly and retain their volatiles within shock melt glass. A mechanism for preserving the signature of martian low-temperature alteration materials within Tissint is therefore as follows: the rock crystallized at relatively low oxygen fugacity conditions and was emplaced within the martian crust, possibly as a shallow sill or surface flow (e.g., Chennaoui Aoudjehane et al. 2012). During its residence on Mars, cracks formed within the rock, allowing exposure to the martian atmosphere. The rock was then subjected to secondary, low-temperature alteration, as material derived from the martian near-surface interacts with the rock and imparts a minor volatile-bearing signature, concentrated within fractures. While the nature of this material in Tissint is obscured, it must have resulted from alteration under relatively low water:rock ratios (Chen et al. 2015), and have been in sufficiently low abundance as to only significantly affect water and chlorine concentrations and isotopic compositions, and leaving concentrations of major, minor (e.g., K, S), and trace elements (e.g., REE, F) unmodified. A hypervelocity impact on Mars (presumably the ejection event) causes a shockwave to pass through the

rock, inducing shock metamorphism, including formation of high-pressure phases and generation of local shock melt as pockets and veins, including via void collapse. Energy released by void collapse generates heat, locally melting portions of the rock; the volatile-bearing material is incorporated into the melt. The relatively oxidizing conditions within the melt cause the formation of hematite from pyrrhotite within shock melt pockets. In Tissint, the near-surface, H_2O-, Cl-rich component is preferentially preserved where the shock melt is quenched to glass, vesicle-free, and isolated from the influence of nearby shock melt pockets or veins where overlapping thermal haloes may extend cooling times and hence devolatilization; similar inferences could be made for other martian meteorites, assuming the presence of martian volatile-bearing alteration material. In the case of Tissint, after ejection from Mars and traversing to Earth, the meteorite was witnessed as a fireball, fell into a hot desert, and remained unaffected by terrestrial weathering prior to collection, thus preserving a unique record of martian low-temperature alteration.

ACKNOWLEDGEMENTS

This study was carried out as a Master's Thesis study by CRK. Financial support for this project was provided by Natural Sciences and Engineering Research Council (NSERC) of Canada Discovery Grant RES00007057 awarded to ELW, NSERC Discovery Grant 261740 awarded to CDKH, and the ASTRO program of the Canadian Space Agency. We gratefully acknowledge the use of the SIMS facilities within the Caltech Microanalysis Center. We thank Andrew Locock and Martin von Dollen at the University of Alberta for expertise in electron microprobe and sample preparation, respectively, Andy DuFrane for assistance with LA-ICP-MS analysis, and Yang Chen for assistance with SIMS analysis. A small portion of this work was performed at JPL, which is managed by Caltech under a contract with NASA. Comments from Sarah Gleeson on the thesis are gratefully acknowledged. We thank Justin Filiberto, two anonymous reviewers and AE Greg Herzog for comments that significantly improved the manuscript.

REFERENCES

Ahrens, T. J., Petersen, C. F., and Rosenberg, J. T., 1969. Shock compression of feldspars. *Journal of Geophysical Research* **74**, 2727-2746.

Avril, C., Malavergne, V., Caracas, R., Zanda, B., Reynard, B., Charon, E., Bobociou, E., Brunet, F., Borensztajn, S., Pont, Sylvain, Tarrida, M., & Guyot, F. (2013). Raman spectroscopic properties and Raman identification of CaS-MgS-MnS-FeS-Cr_2FeS_4 sulfides in meteorites and reduced sulfur-rich systems. *Meteoritics & Planetary Science*, *48*(8), 1415-1426.

Balta, J. B., Sanborn, M. E., Udry, A., Wadhwa, M., & McSween, H. J. (2015). Petrology and trace element geochemistry of Tissint, the newest shergottite fall. *Meteoritics & Planetary Science*, *50*(1), 63-85.

Barrat, J. A., Gillet, P., Lesourd, M., Blichert-Toft, J., & Poupeau, G. R. (1999). The Tatahouine diogenite; mineralogical chemical effects of sixty-three years of terrestrial residence. *Meteoritics & Planetary Science*, *34*(1), 91-97.

Barrat, J.A., Jambon, A., Ferrière, L., Bollinger, C., Langlade, J.A., Liorzou, C., Boudouma, O., & Fialin, M. (2014). No Martian soil component in shergottite meteorites. *Geochimica et Cosmochimica Acta, 125,* 23-33.

Baziotis, I. P., Liu, Y., DeCarli, P. S., Melosh, H. J., McSween, H. Y., Bodnar, R. J., & Taylor, L. A. (2013). The Tissint Martian meteorite as evidence for the largest impact excavation. *Nature Communications, 4*, 1404. doi: 10.1038/ncomms2414.

Beck, P., Ferroir, T., and Gillet, P. (2007) Shock-induced compaction, melting, and entrapment of atmospheric gases in Martian meteorites. Geophysical Research Letters 34, L01203, doi: 10.1029/2006GL028141.

Bouhifd, M., Besson, P., Courtial, P., Gerardin, C., Navrotsky, A., and Richet, P. (2007) Thermochemistry and melting properties of basalt. *Contributions to Mineralogy and Petrology* 153, 689-698.

Chen, Y., Liu, Y., Guan, Y., Eiler, J. M., Ma, C., Rossman, G. R., & Taylor, L. A. (2015). Evidence in Tissint for recent subsurface water on Mars. *Earth and Planetary Science Letters*, *42*, 555-63.

Chennaoui Aoudjehane, H., Avice, G., Barrat, J. A., Boudouma, O., Chen, G., Duke, M. J. M., Franchi, I. A., Gattacceca, J., Grady, M. M., Greenwood, R. C., Herd, C. D. K., Hewins, R., Jambon, A., Marty, B., Rochette, P., Smith, C. L., Sautter, V., Verchovsky, A., Weber, P., & Zanda, B. (2012). Tissint Martian Meteorite: A Fresh Look at the Interior, Surface, and Atmosphere of Mars. *Science*, *338*(6108), 785-788.

Coulson, I. A., Beech, M., and Nie, W. (2007) Physical properties of Martian meteorites; porosity and density measurements. *Meteoritics & Planetary Science* 42, 2043-2054.

Crozaz, G., & Wadhwa, M. (2001). The terrestrial alteration of Saharan shergottites Dar al Gani 476 and 489; a case study of weathering in a hot desert environment. *Geochimica et Cosmochimica Acta*, *65*(6), 971-977.

Crozaz, G., Floss, C., & Wadhwa, M. (2003). Chemical alteration and REE mobilization in meteorites from hot and cold deserts. *Geochimica et Cosmochimica Acta*, *67*(24), 4727-4741.

Dekkers, M. J. (1990). Magnetic monitoring of pyrrhotite alteration during thermal demagnetization. *Geophysical Research Letters*, *17*(6), 779-782.

Feldman, V. I. (1994). The conditions of shock metamorphism. *Special Paper - Geological Society Of America*, *29*, *3*121-132.

Filiberto, J. and Schwenzer, S. P., 2013. Alteration mineralogy of Home Plate and Columbia Hills-Formation conditions in context to impact, volcanism, and fluvial activity. *Meteorit. Planet. Sci.* **48**, 1937-1957.

Greenwood, J. P., Itoh, S., Sakamoto, N., Vicenzi, E. P., & Yurimoto, H. (2008). Hydrogen isotope evidence for loss of water from Mars through time. *Geophysical Research Letters*, *35*(5), CitationL05203. doi:10.1029/2007GL0327.

Hirose, K., and Fei, Y. (2002) Subsolidus and melting phase relations of basaltic composition in the uppermost lower mantle. *Geochimica et Cosmochimica Acta* 66, 2099-2108.

Hu, S., Lin, Y., Zhang, J., Hao, J., Feng, L., Xu, L., Wang, W., & Yang, J. (2014). NanoSIMS analyses of apatite and melt inclusions in the GRV 020090 Martian meteorite: Hydrogen isotope evidence for recent past underground hydrothermal activity on Mars. *Geochimica et Cosmochimica Acta*, *140*, 321-333.

Irving, A. J., Kuehner, S. M., Tanaka, R., Herd, C. D. K., Chen, G., & Lapen, T. J. (2012). The Tissint depleted permafic olivine-phyric shergottite; petrologic, elemental and isotopic characterization of a recent fall in Morocco. *Lunar and Planetary Science XLIII, Houston, Lunar. Planet. Inst, Abstract #2510.*

Jakosky, B. M. and Jones, J. H., 1997. The history of Martian volatiles. *Rev. Geophys.* **35**, 1-16.

Jaret, S. J., Woerner, W. R., Phillips, B. L., Ehm, L., Nekvasil, H., Wright, S. P., and Glotch, T. D., 2015. Maskelynite formation via solid-state transformation: Evidence of infrared and X-ray anisotropy. *J. Geophys. Res.-Planets* **120**, 570-587.

Kieffer, S. W. & Simonds, C. H. (1980). The Role of Volatiles and Lithology in the Impact Cratering Process. *Reviews of Geophysics and Space Physics*, *18*(1), 143-181.

Kubo, T., Kimura, M., Kato, T., Nishi, M., Tominaga, A., Kikegawa, T., & Funakoshi, K. (2010). Plagioclase breakdown as an indicator for shock conditions of meteorites. *Nature Geoscience*, *3*(1), 41-45.

Lafuente, B., Downs, R. T., Yang, H., & Stone, N. (2015). The power of databases: the RRUFF project. *Highlights in Mineralogical Crystallography*, eds. Armbruster, T., & Danisi, R. M. Berlin, Germany, W. De Gruyter, pp 1-30.

Leshin, L. A., Epstein, S., & Stolper, E. M. (1996). Hydrogen isotope geochemistry of SNC meteorites. *Geochimica et Cosmochimica Acta*, *60*(14), 2635-2650.

Liu, Y., Baziotis, I. P., Asimow, P. D., Bodnar, R. J., and Taylor, L. A., 2016. Mineral chemistry of the Tissint meteorite: Indications of two-stage crystallization in a closed system. *Meteorit. Planet. Sci.* **51**, 2293-2315.

Ma, C., Tschauner, O., Beckett, J. R., Liu, Y., Rossman, G. R., Zhuravlev, K., Prakapenka, V., Dera, P., & Taylor, L. A. (2015). Tissintite, (Ca,Na,)$AlSi_2O_6$, a highly-defective, shock-induced, high-pressure clinopyroxene in the Tissint martian meteorite. *Earth and Planetary Science Letters*, *422*, 194-205.

McCubbin, F. M., Boyce, J. W., Srinivasan, P., Santos, A. R., Elardo, S. M., Filiberto, J., Steele, A., and Shearer, C. K., 2016. Heterogeneous distribution of H2O in the Martian interior: Implications for the abundance of H2O in depleted and enriched mantle sources. *Meteorit. Planet. Sci.* **51**, 2036-2060.

Mernagh, T. P., and Trudu, A. G. (1993). A laser Raman microprobe study of some geologically important sulphide minerals. *Chemical Geology*, *103*(1-4), 113-127.

Murase, T., and McBirney, A. R. (1973) Properties of some common igneous rocks and their melts at high temperatures. *Geological Society of America Bulletin* 84, 3563-3592.

Palme, H., Lodders, K., & Jones, A. (2014). Solar system abundances of the elements. In: Holland, H.D., Turekian, K.K. (Eds.), *Treatise on Geochemistry, vol. 2. Second edition*. Elsevier, Oxford, pp. 15–36.

Potts, P. J. (1992) *A Handbook of Silicate Rock Analysis*, Springer, New York, 622 p.

Ross, D. K., Rao, M. N., Nyquist, L. E., Agee, C. B., & Sutton, S. (2013). Compositions of magmatic and impact melt sulfides in Tissint and EETA 79001; precursors of immiscible sulfide melt blebs in shergottite impact melts. *Lunar and Planetary Science XLIV, Houston, Lunar. Planet. Inst, Abstract #1715.*

Rubin, A. E. (2015). Maskelynite in basaltic meteorites; an indicator of shock pressure during impact ejection from parent bodies. *Lunar and Planetary Science XLVI, Houston, Lunar. Planet. Inst, Abstract #1047.*

Schrader, C. M., Cohen, B. A., Donovan, Vicenzi E. P. (2016) Ni/S/Cl systematics and the origin of impact-melt glasses in Martian meteorite Elephant Moraine 79001. *Meteoritics & Planetary Science*, *51*(4), 663-680.

Schwenzer, S. P. and Kring, D. A., 2009. Impact-generated hydrothermal systems capable of forming phyllosilicates on Noachian Mars. *Geology* **37**, 1091-1094.

Schwenzer, S. P. and Kring, D. A., 2013. Alteration minerals in impact-generated hydrothermal systems - Exploring host rock variability. *Icarus* **226**, 487-496.

Sharp, T. G., & DeCarli, P. S. (2006). Shock effects in meteorites. *Meteorites and the early solar system II*, 653-677.

Shaw, C. J., & Walton, E. (2013). Thermal modeling of shock melts in Martian meteorites; implications for preserving Martian atmospheric signatures and crystallization of high-pressure minerals from shock melts. *Meteoritics & Planetary Science*, *48*(5), 758-770.

Sutton, S. R., Ross, D. K., Rao, M. N., & Nyquist, L. E. (2014). Identification of Martian regolith sulfur components in shergottites using sulfur K XANES and Fe/S ratios. *Lunar and Planetary Science XLV, Houston, Lunar. Planet. Inst, Abstract #1524.*

Treiman, A. H., Gleason, J. D., & Bogard, D. D. (2000). The SNC meteorites are from Mars. *Planetary and Space Science 48*, 1213-1230.

Tschauner, O., Ma, C., Beckett, J. R., Prescher, C., Prakapenka, V. B., and Rossman, G. R., 2014. Discovery of bridgmanite, the most abundant mineral in Earth, in a shocked meteorite. *Science* **346**, 1100-1102.

Tyburczy, J. A., Xu, X., Ahrens, T. J., & Epstein, S. (2001). Shock-induced devolatilization and isotopic fractionation of H and C from Murchison Meteorite; some implications for planetary accretion. *Earth and Planetary Science Letters*, *192*(1), 23-30.

Usui, T., Alexander, C. O., Wang, J., Simon, J. I., & Jones, J. H. (2012). Origin of water and mantle-crust interactions on Mars inferred from hydrogen isotopes and volatile element abundances of olivine-hosted melt inclusions of primitive shergottites. *Earth and Planetary Science Letters*, *357-358*, 119-129.

Usui, T., Alexander, C. M. O. D., Wang, J., Simon, J. I., and Jones, J. H., 2015. Meteoritic evidence for a previously unrecognized hydrogen reservoir on Mars. *Earth Planet. Sci. Lett.* **410**, 140-151.

Villanueva, G. L., Mumma, M. J., Novak, R. E., Kaeufl, H. U., Hartogh, P., Encrenaz, T., Tokunaga, A., Khayat, A., & Smith, M. D. (2015). Strong water isotopic anomalies in the Martian atmosphere; probing current and ancient reservoirs. *Science*, *348*(6231), 218-221.

Walton, E. L., & Herd, C. D. K. (2007). Dynamic crystallization of shock melts in Allan Hills 77005: Implications for melt pocket formation in Martian meteorites. *Geochimica et Cosmochimica Acta 71*, 5267–5285.

Walton, E. L., Kelley, S. P., & Spray, J. G. (2007). Shock implantation of Martian atmospheric argon in four basaltic shergottites: A laser probe Ar-40/Ar-39 investigation. *Geochim. Cosmochim. Acta* **71**, 497-520.

Walton, E. L., Jugo, P. J., Herd, C. K., & Wilke, M. M. (2010). Martian regolith in Elephant Moraine 79001 shock melts? Evidence from major element composition and sulfur speciation. *Geochimica et Cosmochimica Acta*, *74*(16), 4829-4843.

Walton, E. L. (2013). Shock metamorphism of Elephant Moraine A79001: Implications for olivine–ringwoodite transformation and the complex thermal history of heavily shocked Martian meteorites. *Geochimica et Cosmochimica Acta 107*, 299–315.

Walton, E. L., Sharp, T. G., Hu, J., & Filiberto, J. (2014). Heterogeneous mineral assemblages in Martian meteorite Tissint as a result of a recent small impact event on Mars. *Geochimica et Cosmochimica Acta, 140*, 334-348.

Wang, W., and Takahashi, E. (1999) Subsolidus and melting experiments of a K-rich basaltic composition to 27 GPa: Implication for the behaviour of potassium in the mantle. *American Mineralogist* 84, 357-361.

Wang, A., Jolliff, B. L., & Haskin, L. A. (1999). Raman spectroscopic characterization of a Martian SNC meteorite: Zagami. *Journal of Geophysical Research*, *104*(E4), 8509-8519.

Wang, A., Kuebler, K. E., Jolliff, B. L., & Haskin, L. A. (2004a). Raman spectroscopy of Fe-Ti-Cr-oxides, case study: Martian meteorite EETA79001. *American Mineralogist*, 89(5-6), 665-680.

Wang, A., Kuebler, K. E., Jolliff, B. L., & Haskin, L. A. (2004b). Mineralogy of a Martian meteorite as determined by Raman spectroscopy. *Journal of Raman Spectroscopy, 35*, 504-514.

Webster, C. R., Mahaffy, P. R., Flesch, G. J., Niles, P. B., Jones, J. H., Leshin, L. A., Atreya, S. K., Stern, J. C., Christensen, L. E., Owen, T., Franz, H., Pepin, R. O., and Steele, A. (2013). Isotope Ratios of H, C, and O in CO_2 and H_2O of the Martian Atmosphere. *Science, 341*, 260-263.

Williams, J. T., C. K. Shearer, Z. D. Sharp, P. V. Burger, F. M. McCubbin, A. R. Santos, C. B. Agee, and K. D. McKeegan (2016), The chlorine isotopic composition of Martian meteorites 1: Chlorine isotope composition of Martian mantle and crustal reservoirs and their interactions, *Meteorit. Planet. Sci.*, In Press.

Wohletz K., Civetta L., & Orsi G. (1999). Thermal evolution of the Phlegraean magmatic system. *Journal of Volcanology and Geothermal Research*, *91*, 391–414.

Figure Captions

Figure 1. BSE images of impact melt in Tissint. A: vesicles in impact melt glass enveloped by glass. B: ringwoodite lamellae within olivine in direct contact with a shock melt pocket. C: tissintite crystals within a clast of plagioclase glass entrained within a quench-crystallized shock melt pocket. D: tissintite within maskelynite in direct contact with shock melt.

Figure 2. Representative Raman spectra for minerals in Tissint. A) Spectra of pyroxene, merrillite and pyrrhotite from the igneous host rock. The spectrum labeled "pyrrhotite + hematite" was obtained from sulfide spherules in shock melt pockets. B) Spectra of ringwoodite and tissintite from shock melt pockets, with spectra from (igneous) olivine and maskelynite for comparison. The maskelynite spectrum was obtained from the core of a grain, while the tissintite spectrum was collected from the boundaries of that grain in contact with a shock melt pocket; the petrologic context is similar to that in Figure 1d.

Figure 3. BSE and X-ray elemental maps of a shock melt pocket in Tissint (section MET11640/2-2-1/TEP). Warmer colors in X-ray maps represent higher concentrations. Scale shown in BSE image applies to all. Schlieren (visible in Ca and Al images) demonstrate the major and minor element compositional heterogeneity of the glass. In contrast, little or no variation is observed in P or Cl images. Fluorine "hotspots" correspond to cracks and holes within the section and are attributable to epoxy.

Figure 4. Histograms of Fe/S ratio for igneous sulfides and sulfide spherules found within impact melt pockets in Tissint (section MET11640/2-3-4/TEP). Fe/S values for sulfide spherules within shock melt pockets are elevated relative to groundmass pyrrhotite. The full dataset is found in the Electronic Annex (Table S3).

Figure 5. Volatile abundances in Tissint shock melt glass as measured by SIMS. Data are derived from analyses within four different shock melt pockets. Error bars (2σ) are given but in

some cases are smaller than the size of the symbol. Chlorine is positively correlated with water (A), and fluorine only weakly so (B). No correlation with water concentration is observed with phosphorus or sulfur (C, E). A combination of water, fluorine, and chlorine is not correlated with phosphorus content (D). The full dataset is found in the Electronic Annex (Table S4).

Figure 6. Isotopic composition and concentration of water in Tissint shock melt glass. Numbered points correspond to SIMS spots within glass labeled in Figure 7. The mixing line is calculated by regressing a line through the data, excluding points labelled 3 and 4; $R^2 = 0.82$. Y intercept = 6925 ‰; X intercept = 0.00685 $1/H_2O$ (146 ppm H_2O) at δD = -100 ‰ (the recommended value for Mars mantle, from Filiberto et al. 2016). "Mars surface water" box encompasses isotopic data from Webster et al. (2013) and Villanueva et al. (2015). "Mars mantle water" box encompass estimates given by Filiberto et al. (2016), ranging up to 200 ppm H_2O ($1/H_2O = 0.005$) and δD = 0 to -100 ‰.

Figure 7. Top: BSE image of a shock melt pocket with vesicles (black, top right). Near the vesicles, the shock melt has quenched to glass. Pits in the glass indicate spots excavated by the primary ion beam during SIMS analysis. Spots indicated by diamonds are plotted in Figure 6. Bottom: traverses through the glass demonstrate that H_2O content in glass decreases with increasing proximity to the large vesicle.

Figure 8. Average CI-chondrite normalized REE abundances for Tissint host (igneous) minerals and shock melt pockets (SMP). Shock melt REE abundances are distinguished based on whether they are crystallite-rich ("SMP crystallites") or glassy ("SMP glass"). Data normalized relative to chondrite abundances from Palme et al. (2014). The full dataset is found in the Electronic Annex (Tables S5, S6).

Figure 9. Top row: digital sketches showing the distribution of shock melt in the three thin sections of Tissint. Bottom row: initial model conditions for shock melt pockets, mapped onto a

0.1 mm grid within the HEAT program. Blue is air, black is shock melt, and white is host rock basalt.

Figure 10. Cooling profiles for three points within a large vesiculated shock melt pocket in Tissint (section MET11640/2-2-1/TEP), as modeled using HEAT. Point A, nearest to the vesicle, cools the fastest, cooling to the solidus in 0.23 s. Further from the vesicle, point B solidifies in 0.57 s. Point C, near the center of a large region of shock melt, cools to the solidus in 0.90 s.

Table 1. Representative compositions of shock melt in Tissint, determined by EPMA and LA-ICP-MS

specimen:	MET11640/2-2-1/TEP				MET11640/2-3-2/TEP				MET11640/2-3-4/TEP	
	glass		crystallites		glass		crystallites		glass	
	average	σ	average	σ	average	σ	average	σ	average	σ
wt%										
SiO_2	48.62	1.17	48.91	2.22	49.83	0.94	49.22	2.18	48.55	1.98
TiO_2	0.45	0.06	0.44	0.16	0.50	0.04	0.49	0.22	b.d.	
Al_2O_3	4.91	3.66	3.29	1.07	4.55	1.09	3.26	1.20	3.77	2.61
Cr_2O_3	0.71	0.15	0.73	0.19	0.60	0.06	0.55	0.14	1.20	
FeO	19.30	2.34	19.18	1.96	18.34	1.07	19.62	2.66	19.25	2.46
MnO	0.55	0.07	0.56	0.04	0.54	0.04	0.58	0.05	0.57	0.05
MgO	17.27	2.40	18.80	2.96	15.50	0.82	17.06	1.78	17.45	2.46
CaO	7.58	0.83	7.31	1.81	8.35	0.71	7.85	1.45	8.28	1.64
Na_2O	0.47	0.41	0.36	0.15	0.66	0.20	0.43	0.18	0.47	0.33
K_2O	0.02	0.01	0.02	0.01	0.04	0.05	0.02	0.01	b.d.	
P_2O_5	0.31	0.09	0.32	0.74	0.25	0.11	0.20	0.09	0.33	0.17
SO_3	0.30	0.11	0.41	0.40	0.47	0.20	0.83	0.73	1.36	0.67
Cl	0.02	0.00	0.02	0.01	-	-	-	-	b.d.	
NiO	0.03	0.01	0.04	0.02	0.03	0.01	0.03	0.01	-	
Total	100.48		100.32		99.62		100.01		98.86	
ppm										
La	0.16		b.d.		b.d.		b.d.		b.d.	
Ce	0.57	0.08	0.57	0.05	b.d.		0.62	0.19	b.d.	
Pr	0.13	0.01	0.13	0.02	b.d.		0.13	0.03	0.13	0.03
Nd	0.80	0.13	0.79	0.09	0.48	0.08	0.83	0.37	0.75	0.12
Sm	0.51	0.10	0.49	0.07	0.4	0.04	0.53	0.14	0.63	0.13
Eu	0.24	0.04	0.23	0.03	0.12	0.02	0.24	0.08	0.33	0.08
Gd	1.08	0.21	1.14	0.29	0.83	0.08	1.06	0.31	1.16	0.24
Tb	0.20	0.02	0.19	0.02	0.16	0.01	0.22	0.06	0.22	0.05
Dy	1.47	0.16	1.39	0.14	1.2	0.09	1.57	0.34	1.71	0.28
Ho	0.33	0.03	0.30	0.02	0.26	0.02	0.35	0.08	0.35	0.06
Er	0.89	0.08	0.87	0.11	0.76	0.10	1.09	0.25	1.08	0.09
Tm	0.13	0.01	0.13	0.01	0.12	0.01	0.14	0.03	0.16	0.02
Yb	0.83	0.08	0.80	0.05	0.75	0.01	0.96	0.20	1.12	0.27
Lu	0.12	0.01	0.15	0.03	0.12	0.01	0.14	0.02	0.14	0.02

Notes: "σ" is the one-sigma standard deviation of the mean, "b.d." indicates measurement below the limit of detection, and "-" indicates not targeted for analysis. The full dataset is found in the Electronic Annex.

Table 2. Representative compositions of shock melt in Tissint, determined by SIMS

sample	H_2O ppm	2σ	F ppm	2σ	Cl ppm	2σ	S ppm	2σ	P_2O_5 wt%	2σ	δD	2σ
234-1	297.6	3.1	11.7	0.1	14.2	0.1	1067.4	6.7	0.257	0.006	3757	49
234-2	278.5	2.3	11.7	0.1	15.9	0.1	1073.2	2.7	0.250	0.006	2913	77
234-3	261.6	2.6	10.3	0.1	11.2	0.2	614.7	9.9	0.166	0.007	4422	67
234-4	373.9	6.1	10.9	0.1	13.5	0.1	809.7	10.6	0.196	0.008	3831	38
234-5	329.9	4.6	10.2	0.1	11.3	0.1	715.3	6.3	0.161	0.006	4007	56
234-6	353	4.2	10.8	0.1	19.9	0.2	288.2	3.9	0.105	0.002	4232	53
234-7	266.9	2.6	11.5	0.1	16.1	0.1	1075	9.1	0.295	0.014	4325	57
234-8	234.3	3.6	9.6	0.1	28.2	1.6	573.6	22.8	0.148	0.003	2559	89

Notes: all data obtained from specimen MET11640/2-3-4/TEP. The full dataset is found in the Electronic Annex.

Kuchka et al. Figure 1

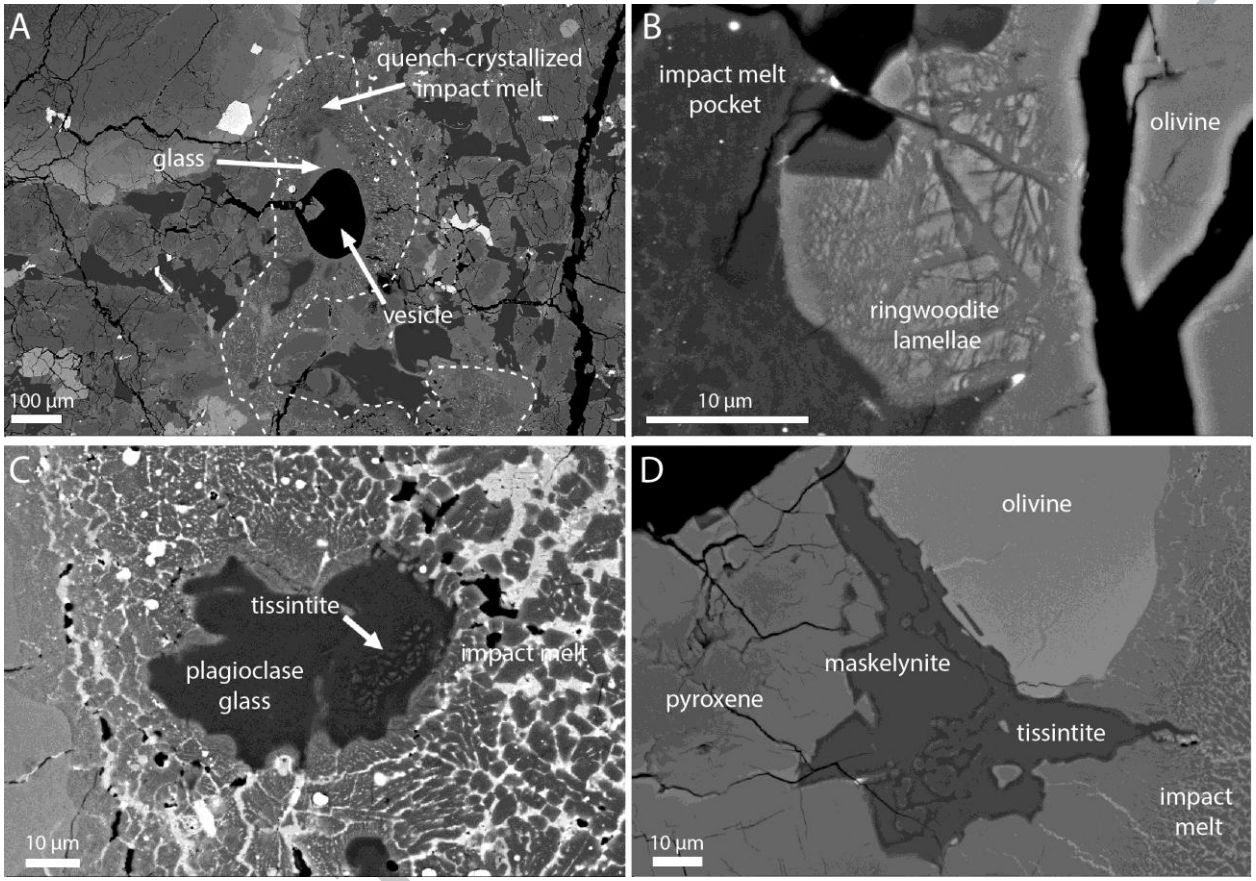

Figure 1. BSE images of impact melt in Tissint. A) vesicles in impact melt glass enveloped by glass. B) ringwoodite lamellae within olivine in direct contact with a shock melt pocket. C) tissintite crystals within a clast of plagioclase glass entrained within a quench-crystallized shock melt pocket. D) tissintite within maskelynite in direct contact with shock melt.

Kuchka et al. Figure 2

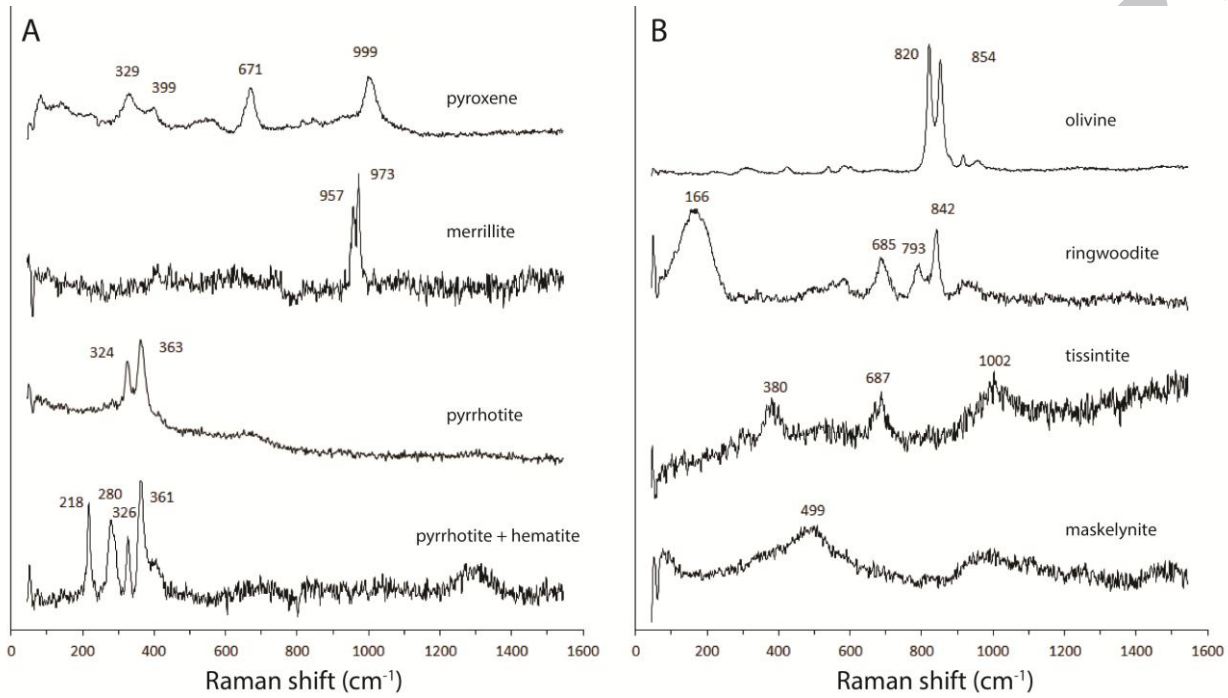

Figure 2. Representative Raman spectra for minerals in Tissint. A) Spectra of pyroxene, merrillite and pyrrhotite from the igneous host rock. The spectrum labeled "pyrrhotite + hematite" was obtained from sulfide spherules in shock melt pockets. B) Spectra of ringwoodite and tissintite from shock melt pockets, with spectra from (igneous) olivine and maskelynite for comparison. The maskelynite spectrum was obtained from the core of a grain, while the tissintite spectrum was collected from the boundaries of that grain in contact with a shock melt pocket; the petrologic context is similar to that in Figure 1d.

Kuchka et al. Figure 3

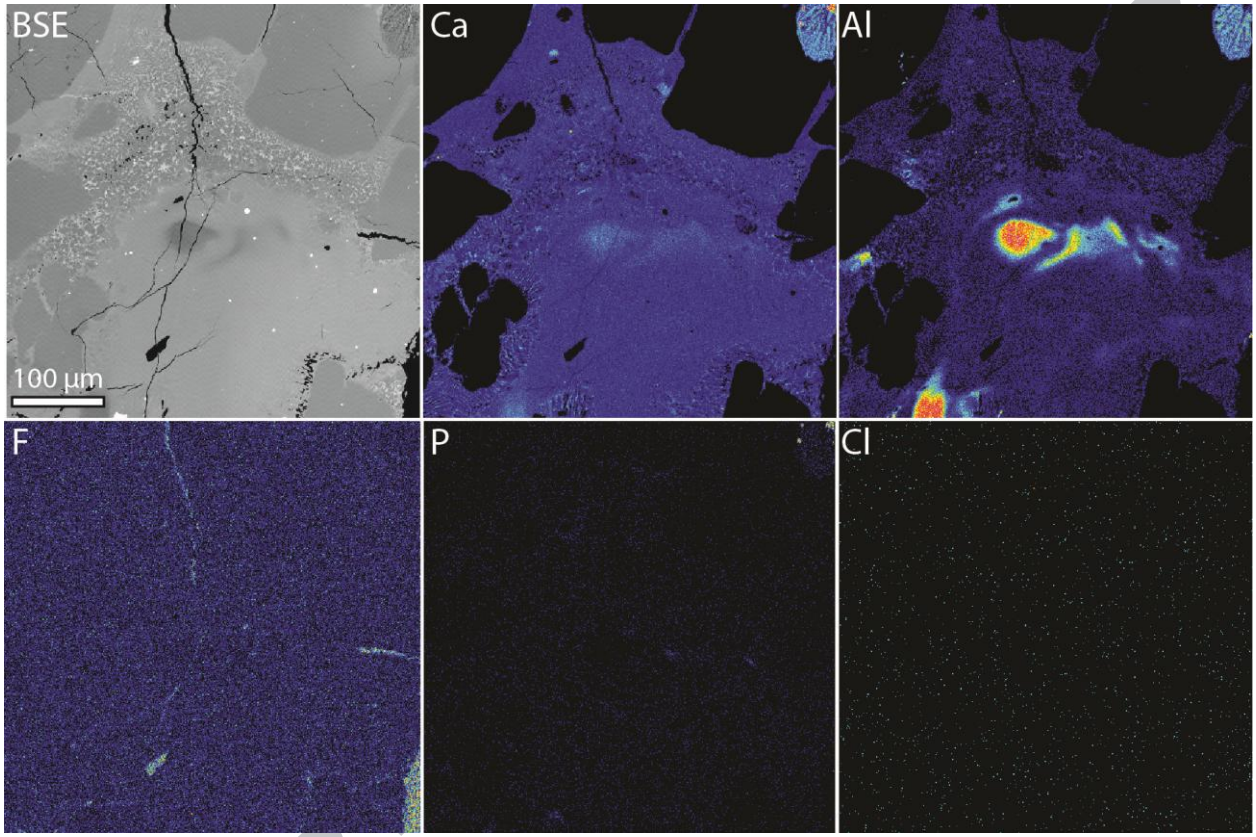

Figure 3. BSE and X-ray elemental maps of a shock melt pocket in Tissint (section MET11640/2-2-1/TEP). Warmer colors in X-ray maps represent higher concentrations. Scale shown in BSE image applies to all. Schlieren (visible in Ca and Al images) demonstrate the major and minor element compositional heterogeneity of the glass. In contrast, little or no variation is observed in P or Cl images. Fluorine "hotspots" correspond to cracks and holes within the section and are attributable to epoxy.

Kuchka et al. Figure 4

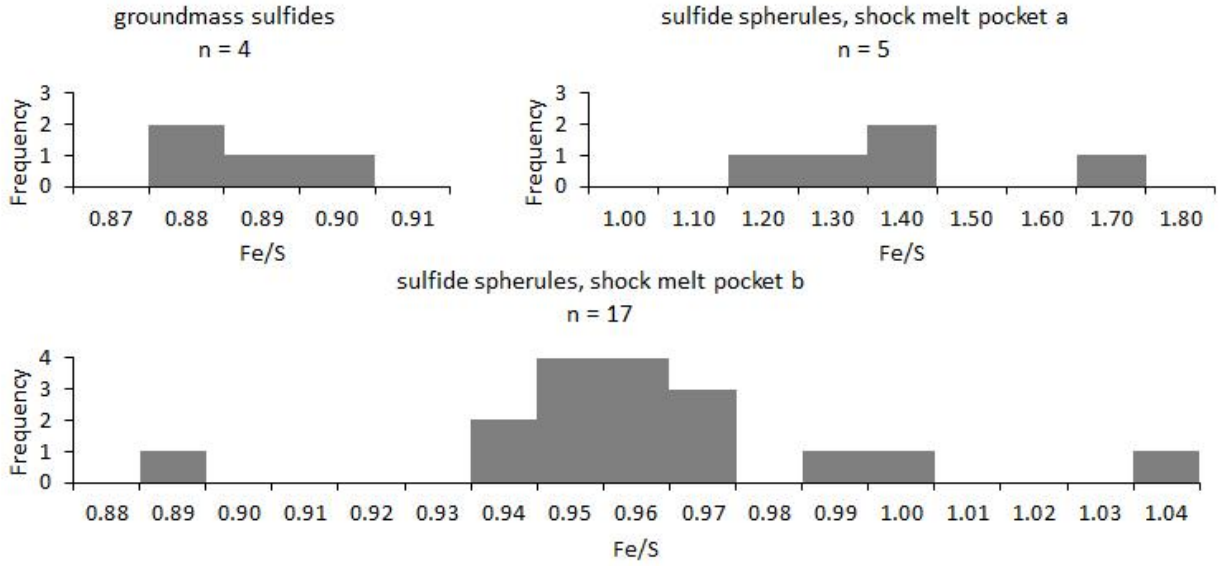

Figure 4. Histograms of Fe/S ratio for igneous sulfides and sulfide spherules found within impact melt pockets in Tissint (section MET11640/2-3-4/TEP). Fe/S values for sulfide spherules within shock melt pockets are elevated relative to groundmass pyrrhotite. The full dataset is found in the Electronic Annex (Table S3).

Kuchka et al. Figure 5

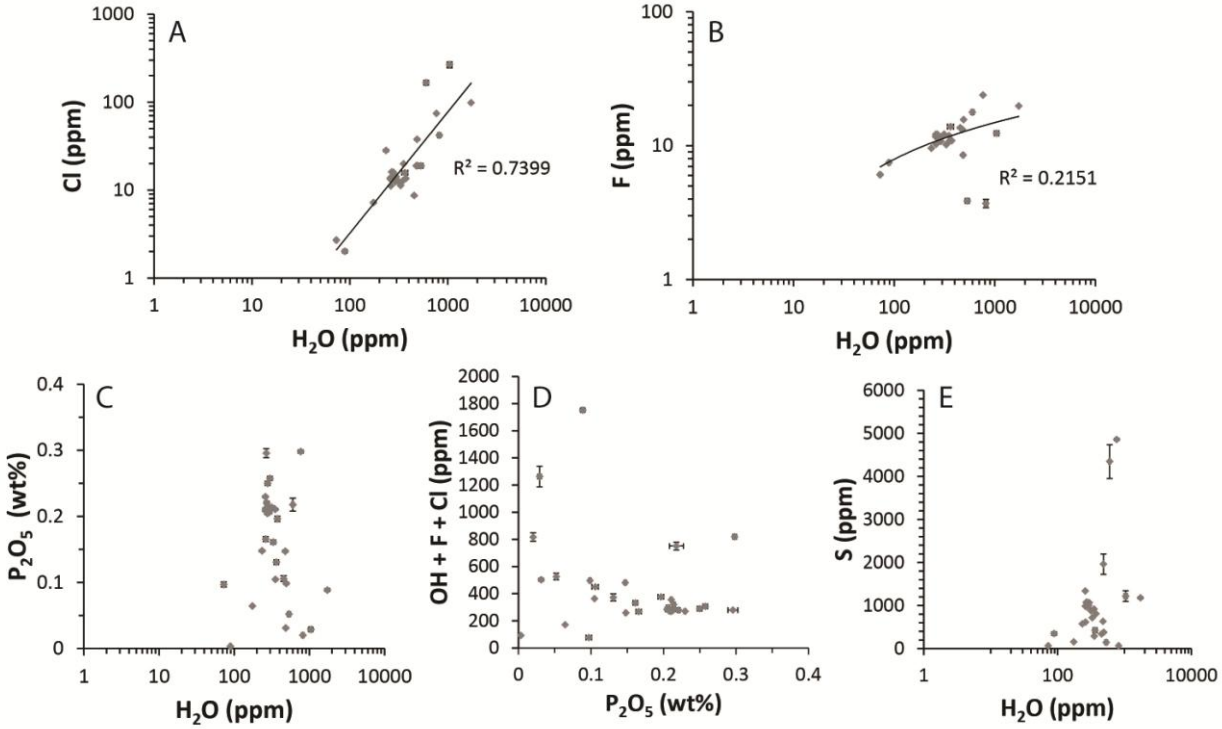

Figure 5. Volatile abundances in Tissint shock melt glass as measured by SIMS. Data are derived from analyses within four different shock melt pockets. Error bars (2σ) are given but in some cases are smaller than the size of the symbol. Chlorine is positively correlated with water (A), and fluorine only weakly so (B). No correlation with water concentration is observed with phosphorus or sulfur (C, E). A combination of water, fluorine, and chlorine is not correlated with phosphorus content (D). The full dataset is found in the Electronic Annex (Table S4).

Kuchka et al. Figure 6

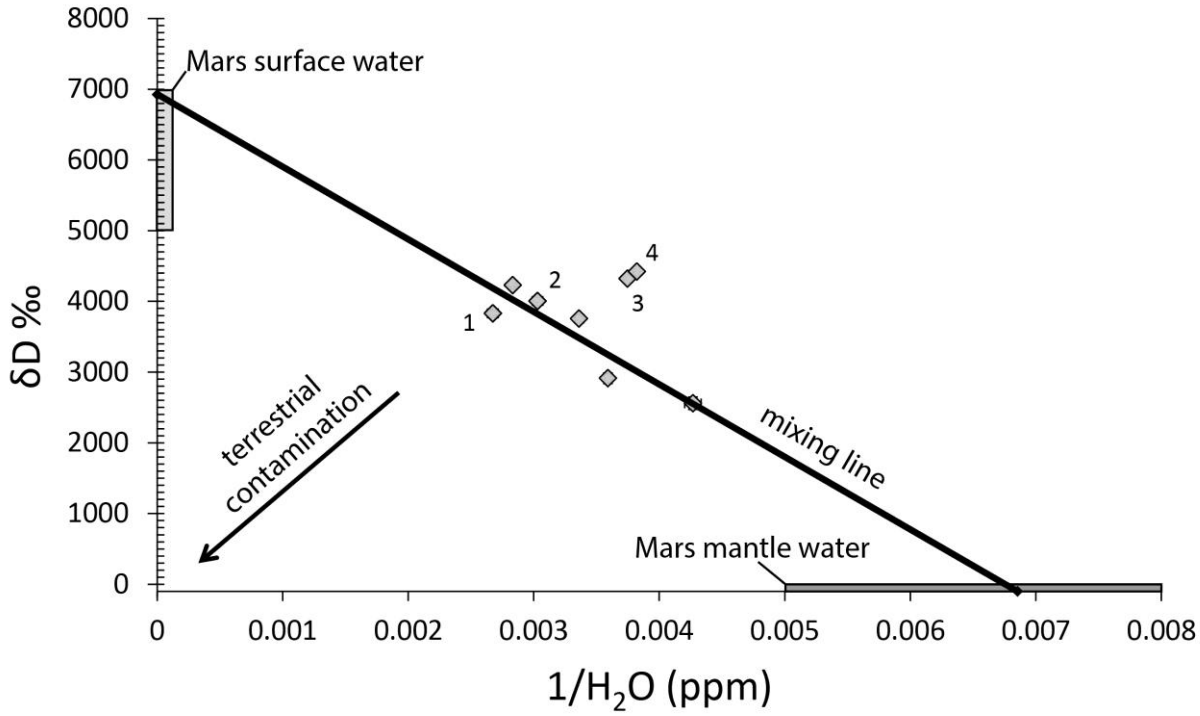

Figure 6. Isotopic composition and concentration of water in Tissint shock melt glass. Numbered points correspond to SIMS spots within glass labeled in Figure 7. The mixing line is calculated by regressing a line through the data, excluding points labelled 3 and 4; R^2 = 0.82. Y intercept = 6925 ‰; X intercept = 0.00685 $1/H_2O$ (146 ppm H_2O) at δD = -100 ‰ (the recommended value for Mars mantle, from Filiberto et al. 2016). "Mars surface water" box encompasses isotopic data from Webster et al. (2013) and Villanueva et al. (2015). "Mars mantle water" box encompass estimates given by Filiberto et al. (2016), ranging up to 200 ppm H_2O ($1/H_2O$ = 0.005) and δD = 0 to -100 ‰.

Kuchka et al. Figure 7

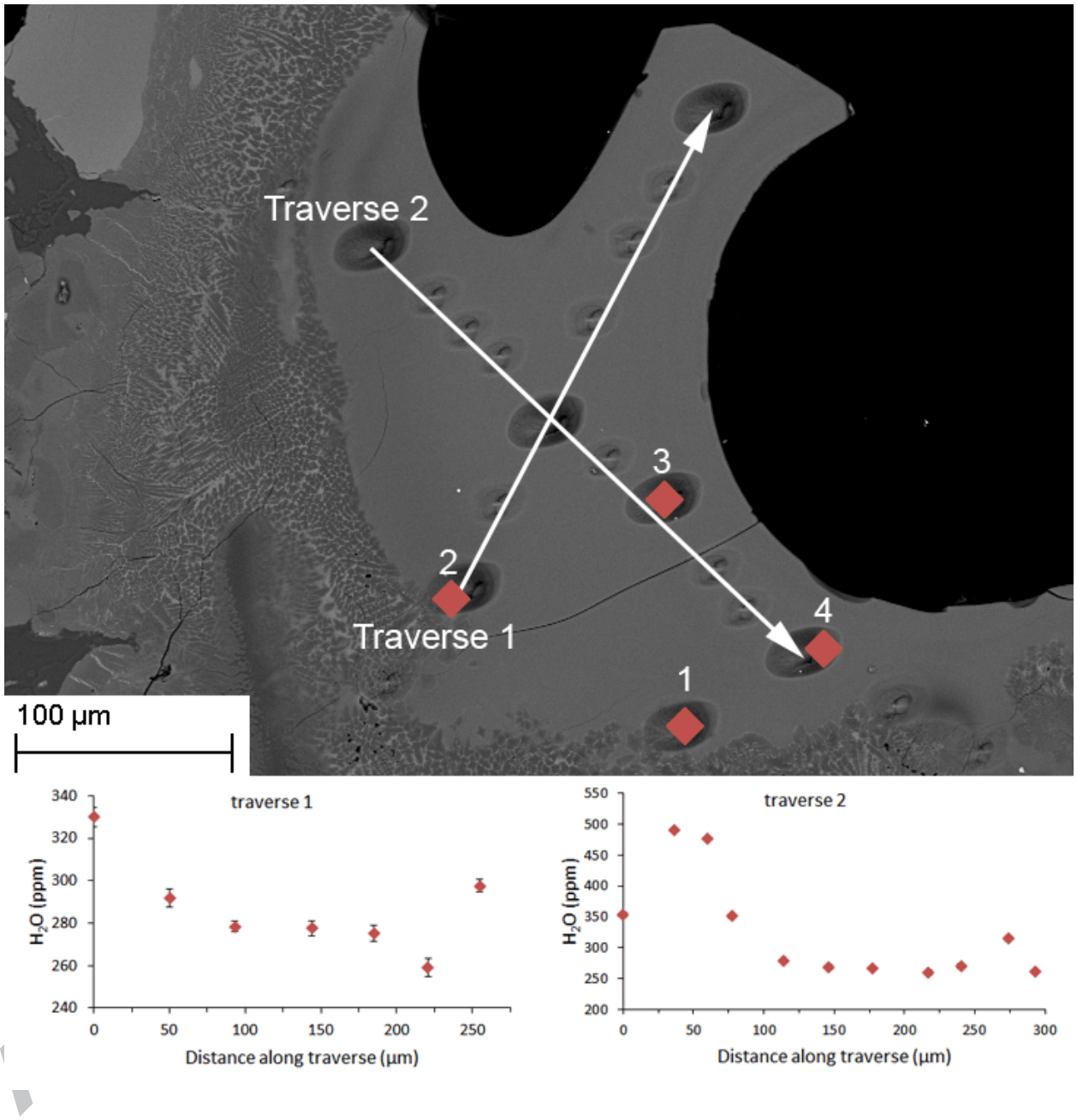

Figure 7. Top: BSE image of a shock melt pocket with vesicles (black, top right). Near the vesicles, the shock melt has quenched to glass. Pits in the glass indicate spots excavated by the primary ion beam during SIMS analysis. Spots indicated by diamonds are plotted in Figure 6. Bottom: traverses through the glass demonstrate that H_2O content in glass decreases with increasing proximity to the large vesicle.

Kuchka et al. Figure 8

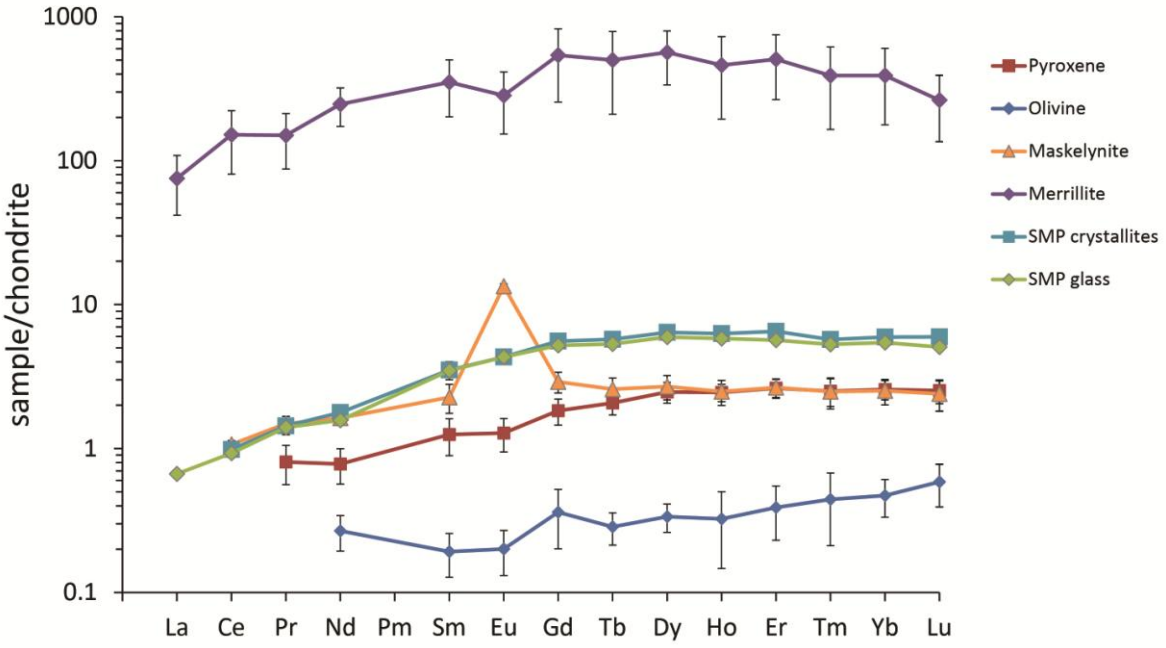

Figure 8. Average CI-chondrite normalized REE abundances for Tissint host (igneous) minerals and shock melt pockets (SMP). Shock melt REE abundances are distinguished based on whether they are crystallite-rich ("SMP crystallites") or glassy ("SMP glass"). Data normalized relative to chondrite abundances from Palme et al. (2014). The full dataset is found in the Electronic Annex (Tables S5, S6).

Kuchka et al. Figure 9

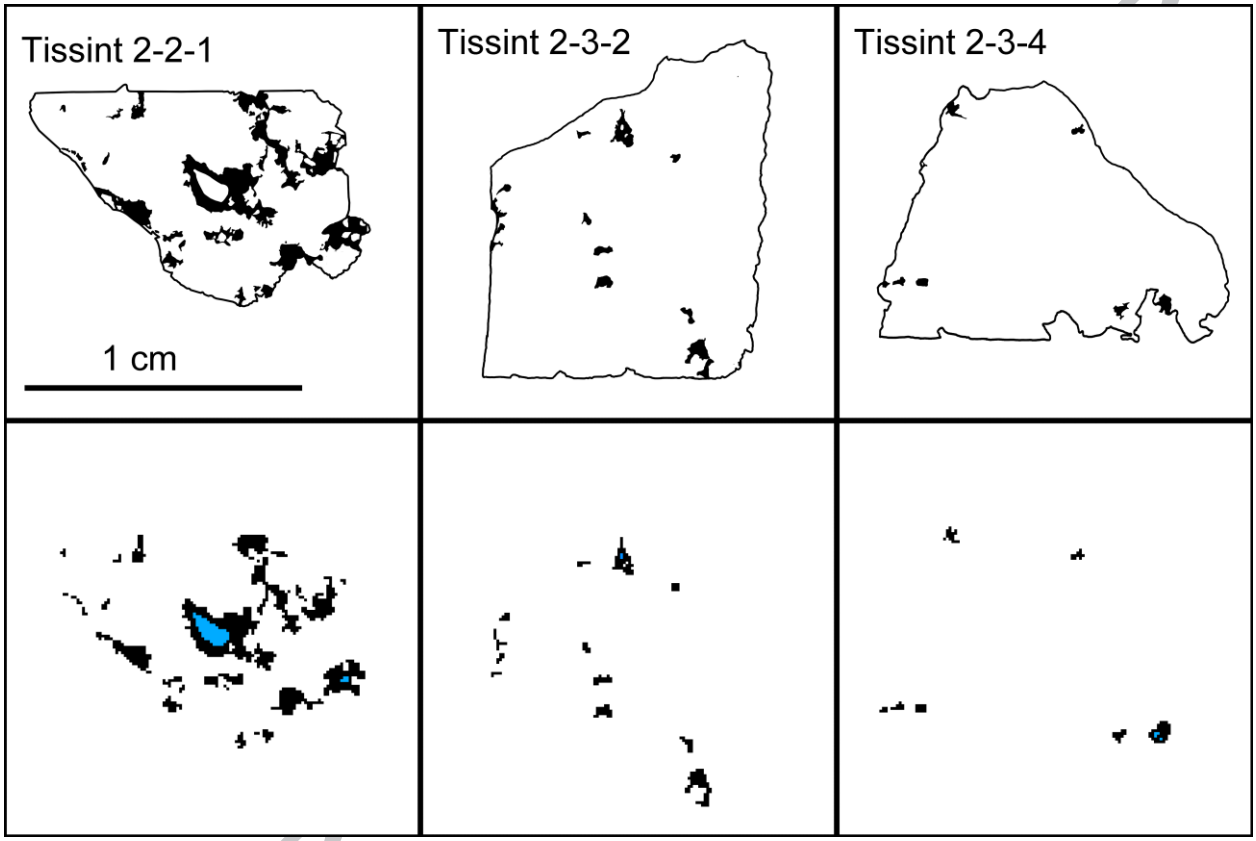

Figure 9. Top row: digital sketches showing the distribution of shock melt in the three thin sections of Tissint. Bottom row: initial model conditions for shock melt pockets, mapped onto a 0.1 mm grid within the HEAT program. Blue is air, black is shock melt, and white is host rock basalt.

Kuchka et al. Figure 10

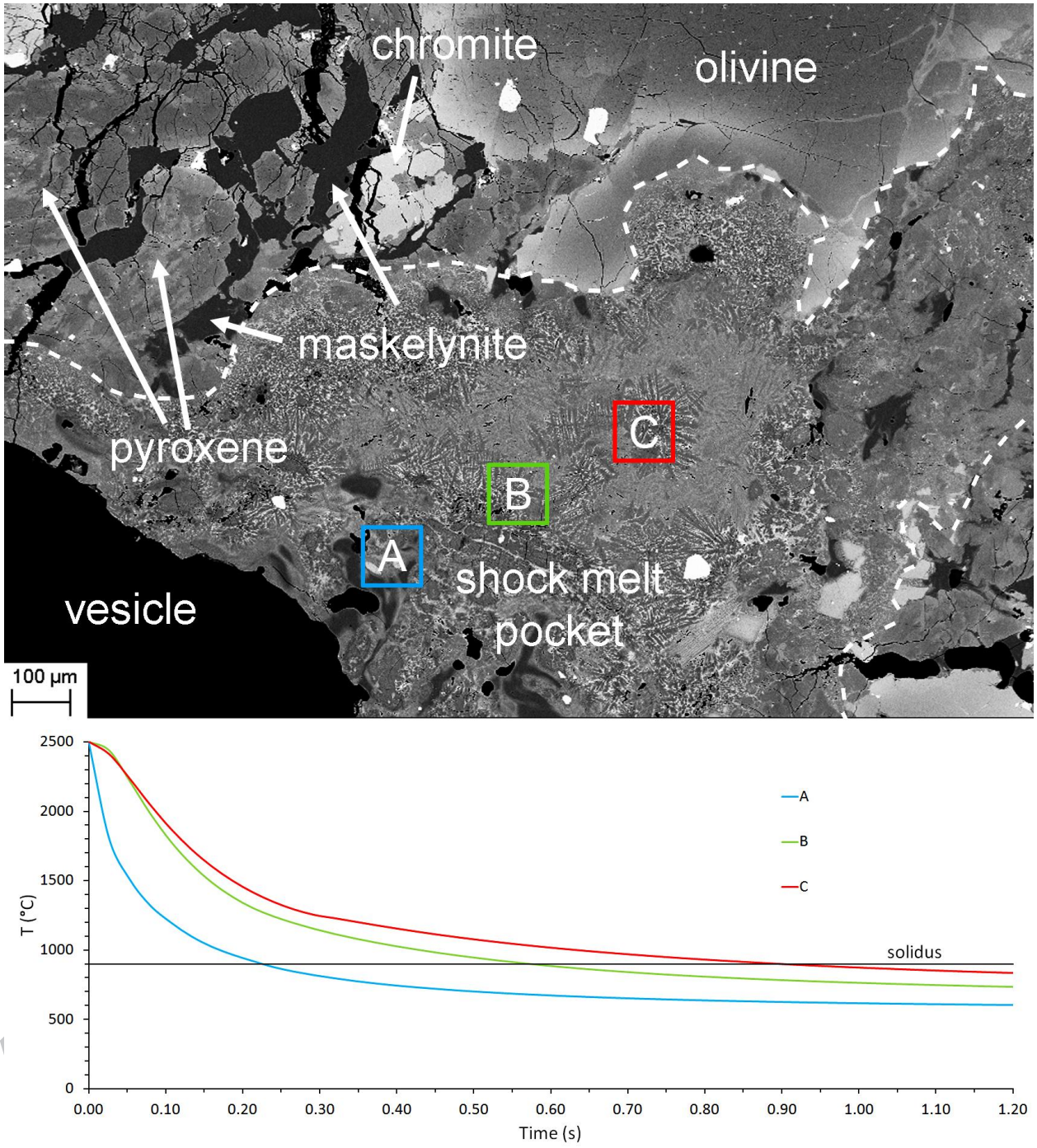

Figure 10. Cooling profiles for three points within a large vesiculated shock melt pocket in Tissint (section MET11640/2-2-1/TEP), as modeled using HEAT. Point A, nearest to the vesicle, cools the fastest, cooling to the solidus in 0.23 s. Further from the vesicle, point B solidifies in 0.57 s. Point C, near the center of a large region of shock melt, cools to the solidus in 0.90 s.